



1 Estimating 2010–2015 Anthropogenic and Natural Methane 2 Emissions in Canada using ECCC Surface and GOSAT Satellite 3 Observations

4 Sabour Baray¹, Daniel J. Jacob², Joannes D. Maasakkers³, Jian-Xiong Sheng⁴, Melissa P. Sulprizio²,
5 Dylan B.A. Jones⁵, A. Anthony Bloom⁶, and Robert McLaren¹

6 ¹Centre for Atmospheric Chemistry, York University, Toronto, Canada

7 ²Harvard University, Cambridge, MA, USA

8 ³SRON Netherlands Institute for Space Research, Utrecht, The Netherlands

9 ⁴Massachusetts Institute of Technology, Cambridge, MA, USA

10 ⁵University of Toronto, Toronto, Canada

11 ⁶Jet Propulsion Laboratory, California Institute of Technology, Pasadena, CA, USA

12 *Correspondence to:* Sabour Baray (sabour@yorku.ca)

13 **Abstract.** Methane emissions in Canada have both anthropogenic and natural sources. Anthropogenic emissions are estimated to be
14 4.1 Tg a⁻¹ from 2010–2015 in the Canadian Greenhouse Gas Inventory. Natural emissions, which are mostly due to Boreal wetlands,
15 are the largest methane source in Canada and highly uncertain, on the order of ~20 Tg a⁻¹ in biosphere process models. Top-down
16 constraints on Canadian methane emissions using atmospheric observations have been limited by the sparse coverage of both surface
17 and satellite observations. Aircraft studies over the last several years have provided ‘snapshot’ emissions that have been conflicting
18 with inventory estimates. Here we use surface data from the Environment and Climate Change Canada (ECCC) in situ network and
19 space borne data from the Greenhouse Gases Observing Satellite (GOSAT) to determine 2010–2015 anthropogenic and natural
20 methane emissions in Canada in a Bayesian inverse modelling framework. We use GEOS-Chem to simulate anthropogenic emissions
21 comparable to the Canadian inventory and wetlands emissions using an ensemble of WetCHARTS v1.0 scenarios in addition to other
22 minor natural sources. We conduct a comparative analysis of the monthly natural emissions and yearly anthropogenic emissions
23 optimized by surface and satellite data independently. Mean 2010–2015 posterior emissions using ECCC surface data are 6.0 ± 0.4
24 Tg a⁻¹ for total anthropogenic and 10.5 ± 1.9 Tg a⁻¹ for total natural emissions, where the error intervals represent the 1-σ spread in
25 yearly posterior results. These results agree with our posterior using GOSAT data of 6.5 ± 0.7 Tg a⁻¹ for total anthropogenic and 11.7
26 ± 1.2 Tg a⁻¹ for total natural emissions. The seasonal pattern of posterior natural emissions using either dataset shows slower to start
27 emissions in the spring and a less intense peak in the summer compared to the mean of WetCHARTS scenarios. We combine ECCC
28 and GOSAT data to evaluate capabilities for sectoral and provincial level inversions and identify limitations. We estimate Energy +
29 Agriculture emissions to be 5.1 ± 1.0 Tg a⁻¹ which is 59% higher than the National GHG Inventory. We attribute 39% higher
30 anthropogenic emissions to Western Canada than the prior. Natural emissions are lower across Canada with large downscaling in the
31 Hudson Bay Lowlands. Inversion results are verified against independent aircraft data in Saskatchewan and surface data in Quebec
32 which show better agreement with posterior emissions. This study shows a readjustment of the Canadian methane budget is necessary
33 to better match atmospheric observations with higher anthropogenic emissions partially offset by lower natural emissions.



34 1 Introduction

35 Methane is a significant greenhouse gas second to carbon dioxide in terms of its direct radiative forcing (Myhre et al., 2013).
36 The mixing ratio of methane has increased from ~720 to ~1800 ppb since pre-industrial times (Hartmann et al., 2013). Present-
37 day global methane emissions are well known to be $550 \pm 60 \text{ Tg a}^{-1}$ (Prather et al., 2012), however recent trends in atmospheric
38 methane since the 1990s are not well understood (Turner et al., 2019). Anthropogenic methane sources include oil and gas
39 activities, livestock, rice cultivation, coal mines, landfills, and wastewater treatment. Natural methane emissions are dominated
40 by wetlands, but also include seeps, termites and biomass burning (Kirschke et al., 2013). The main sink of methane is
41 oxidation by the hydroxyl radical (OH) resulting in a lifetime of 9.1 ± 0.9 years (Prather et al., 2012). Improving constraints
42 on national methane emissions is a requirement of mitigation policy (Nisbet et al., 2020). Here we use atmospheric methane
43 observations from the Environment and Climate Change Canada (ECCC) surface network and satellite observations from the
44 Greenhouse Gas Observing Satellite (GOSAT) to estimate Canadian methane emissions and disaggregate anthropogenic and
45 natural sources.

46

47 The growth rate of atmospheric methane levelled off from the 1990's to early 2000's. This hiatus continued until 2007 when
48 methane concentrations began a renewed growth continuing to present time (Dlugokencky et al., 2009). Differing hypotheses
49 have attempted to constrain the possible causes of these decadal trends. Associated increases with ethane have attributed recent
50 growth to oil and gas (Hausmann et al., 2016). An increasing trend of isotopically lighter methane has been associated with
51 increasing biogenic emissions from wetlands and agriculture (Nisbet et al., 2016), however decreasing biomass burning
52 emissions may be masking increasing oil and gas emissions in the global isotopic ratios (Worden et al., 2017). Observations
53 of methyl chloroform suggest decreasing OH may have resulted in the renewed growth (Rigby et al., 2017; Turner et al., 2017).
54 Causal attribution of the methane growth rate has continued to be challenging partly because only a 3% source-sink imbalance,
55 or $\sim 20 \text{ Tg a}^{-1}$, can result in the observed rate of increase. Hence changes in the relative contributions from anthropogenic and
56 natural sources are key to understanding atmospheric methane.

57

58 Atmospheric observations provide constraints on methane emissions. In the Canadian greenhouse gas inventory, anthropogenic
59 emissions are estimated to be 4.1 Tg a^{-1} in 2015 with 68% of emissions originating from the Western Canadian provinces of
60 Alberta (42%), Saskatchewan (17%) and British Columbia (9%). Sectoral contributions over the entire country are from three
61 categories: Energy (49%), Agriculture (29%) and Waste (22%) (Environment and Climate Change Canada, 2017). Natural
62 emissions, which are mostly due to Boreal wetlands, are highly uncertain, on the order of $\sim 10\text{-}30 \text{ Tg a}^{-1}$ from biosphere process
63 modelling (Miller et al., 2014; Bloom et al., 2017). Studies constraining anthropogenic and/or natural methane emissions
64 within Canada have included the use of surface in situ measurements (Miller et al., 2016; Atherton et al., 2017; Ishiziwa et al.,
65 2019), aircraft campaigns (Johnson et al., 2017; Baray et al., 2018) and satellites (Wecht et al., 2014; Turner et al., 2015;
66 Maasackers et al., 2020). These observations can determine emissions through mass balance methods or be used in conjunction



67 with a chemical transport model (CTM). Bayesian inverse modelling constrains prior knowledge of emissions based on the
68 mismatch between modelled and observed concentrations. This requires reliable mapping of “bottom-up” inventory emissions
69 for the “top-down” observational constraints to be useful (Jacob et al., 2016). Inverse modelling has been more challenging
70 for Canada than the United States due to a) the sparsity of surface stations and satellite data (Sheng et al., 2018a), b) a factor
71 of ~10 lower anthropogenic emissions (Maasackers et al., 2019), c) large spatially-overlapping emissions from Boreal wetlands
72 that are highly uncertain (Miller et al., 2014), and d) model biases in the high-latitudes stratosphere (Patra et al., 2011),
73 compromising interpretation of observed methane columns.

74

75 These observing system challenges have made Canadian methane emissions difficult to quantify, however studies have been
76 showing a consistent story across different scales and measurement platforms. Miller et al. (2014, 2016) determined that the
77 North American network can successfully constrain Canadian natural emissions and found Boreal wetlands to be lower in
78 2008 when compared to prior fluxes in the WETCHIMP model. Aircraft campaigns over the Alberta oil and gas sector have
79 found higher emissions than inventories in the Red Deer and Lloydminster regions (Johnson et al., 2017) and unconventional
80 oil extraction in the Athabasca Oil Sands region (Baray et al., 2018). Atherton et al. (2017) conducted ground-based mobile
81 measurements of gas production in British Columbia and determined higher emissions than reported, and Zavala-Araiza et al.
82 (2018) conducted similar ground-based measurements in Alberta to show a profile of super-emitters dominating the fugitive
83 methane profile similar to sites in the United States. Ishiziwa et al. (2019) constrained arctic wetlands fluxes to be similar in
84 magnitude to the mean of the WetCHARTS inventory but with better identified seasonal and interannual variability. Satellite
85 inversions over North America using the GEOS-Chem CTM and data from SCIAMACHY (Wecht et al., 2014) or GOSAT
86 (Turner et al., 2015; Maasackers et al., 2019) consistently require upscaling anthropogenic emissions in Western Canada and
87 downscaling natural emissions in Boreal Canada to match observations, even with the use of updated Canadian fluxes in
88 Maasackers et al. (2019) for anthropogenic (Sheng et al., 2017) and wetlands (Bloom et al., 2017) sources. Inverse modelling
89 studies that use both in situ and satellite observations are valuable for intercomparison and for identifying the limits of spatial
90 and temporal discretization that are possible (Lu et al., 2020; Tunnicliffe et al., 2020). The Tropospheric Monitoring Instrument
91 (TROPOMI) launched in 2017 with a data record beginning in 2018 and is expected to provide significant improvements in
92 emissions monitoring through denser observational coverage at a similar precision to GOSAT (Hu et al., 2018). It is necessary
93 to build a reliable historical record of Canadian methane emissions as anthropogenic emissions are sensitive to changes in
94 policy and economic activity (Rogelj et al., 2018) and natural emissions in Boreal Canada may be sensitive to climate change
95 (Kirschke et al., 2013).

96

97 In this study we use surface observations from the ECCC GHG monitoring network and satellite data from GOSAT to constrain
98 anthropogenic and natural emissions in Canada. We use the GEOS-Chem CTM to simulate 2010–2015 methane
99 concentrations. The model setup includes the use of an improved bottom-up inventory for Canadian oil and gas emissions
100 (Sheng et al., 2017), the WetCHARTS extended ensemble for wetlands emissions (Bloom et al., 2017) and EDGAR v4.3.2 for



101 other anthropogenic sources. We perform an ensemble forward model analysis which compares six wetlands scenarios to the
102 ECCC surface observation network to assess the influence of process model configurations on Canadian methane. A series of
103 Bayesian inverse analyses are performed that use ECCC and GOSAT data independently and in a joint surface-satellite system.
104 We constrain monthly natural emissions and yearly total anthropogenic emissions from 2010–2015 using ECCC and GOSAT
105 data independently for intercomparison to produce aggregated-source emissions estimates. We test the limitations of the
106 ECCC and GOSAT joint observation system towards constraining emissions by inventory sector and according to provincial
107 boundaries. We demonstrate where the observation system succeeds in providing strong constraints on major emissions sources
108 and quantify the information content of the system to understand the limitations for resolving all minor Canadian emissions.

109 **2 Data and Methods**

110 We use the GEOS-Chem CTM v12-03 (<http://acmg.seas.harvard.edu/geos/>) to simulate methane fields from 2010–2015 on a
111 $2^\circ \times 2.5^\circ$ global grid and compare to surface observations from the ECCC in situ GHG monitoring network and satellite
112 observations from GOSAT within the Canadian domain. We test for bias in the global model representation of background
113 methane using both surface and aircraft in situ data at Canada’s most westerly site Estevan Point (ESP) and using global
114 GOSAT data. The sensitivity of simulated methane in Canada to the use of different wetlands flux parametrization is evaluated
115 by comparing an ensemble of WetCHARTS v1.0 configurations to ECCC surface observations. The WetCHARTS ensemble
116 mean along other GEOS-Chem prior emissions are used in the Bayesian inverse analysis which optimizes Canadian sources
117 using ECCC surface data and GOSAT satellite data independently for comparative analysis. We show the limitations of the
118 observing system towards subnational level discretization by combining ECCC and GOSAT data in a joint-inversion. Here we
119 describe the observations, the model, and the inverse analysis in further detail.

120 **2.1 Observations**

121 **2.1.1 In situ Surface Observations**

122 We use continuous measurements from eight sites in the ECCC greenhouse gas monitoring network from 2010–2015. Figure
123 1 shows a map of the sites and Table 1 provides a descriptive list. The eight sites are Estevan Point, British Columbia (ESP),
124 Lac La Biche, Alberta (LLB), East Trout Lake, Saskatchewan (ETL), Churchill, Manitoba (CHC), Fraserdale, Ontario (FRA),
125 Egbert, Ontario (EGB), Chibougamau, Quebec (CHM) and Sable Island, Nova Scotia (SBL). All sites use Picarro cavity ring-
126 down spectrometers (G1301, G2301 or G2401) measuring dry-air mol fractions of methane with hourly-average precision
127 better than 1 ppb. For model comparison the measurements are averaged over 4h from 12:00 to 16:00 local time for when the
128 planetary boundary layer is well-mixed. The instruments are calibrated against World Meteorological Organization (WMO)
129 certified standard gases. The western most site, ESP, measures methane continuously from a 40 m tower at a lighthouse station
130 on the west coast of Vancouver Island. ESP is surrounded by forests to the north, east, and south and the Pacific Ocean to the
131 west. ESP is used to evaluate boundary conditions and model bias in the methane background as it is the least sensitive to



132 Canadian emissions due to prevailing westerly winds. Sites LLB and ETL are the most sensitive to anthropogenic emissions
133 in Western Canada. LLB measures continuously from a 50 m tower located in a region of peatlands and forest ~200 km NE
134 of Edmonton and ~230 km S of Fort McMurray. ETL measures from a height of 105 m located ~150 km north of Prince Albert
135 surrounded by Boreal forest. The sites in the Hudson Bay Lowlands (HBL) region, CHC and FRA, are the most sensitive to
136 natural wetlands emissions as this area produces some of the largest methane fluxes in North America. CHC measures
137 continuously from a 60 m tower in a small port town on the western edge of Hudson Bay surrounded by flat tundra. FRA
138 measures from a 40 m tower and is located on the southern perimeter of James Bay surrounded by extensive wetlands coverage.
139 The site CHM in Quebec is also sensitive to natural wetlands emissions and is excluded in the inverse analysis to be used to
140 verify the posterior results. CHM is substituted by Chapais, Quebec ~50 km away from 2011 onwards. The remaining Central
141 and Atlantic Canada sites EGB and SBL are sensitive to net outflow from Canadian sources, both natural and urban, and some
142 emissions from the Eastern United States. EGB is in a small rural village ~80 km north of Toronto and measures from a 25 m
143 tower. SBL is on a remote uninhabited island 275 km ESE of Halifax, Nova Scotia and measures from a height of 25 m.

144
145 **Table 1:** Descriptive list of ECCC in situ observation sites used in the analysis.
146

Site Code	Full Name, Province	Latitude	Longitude	Elevation (asl) / Sampling Height (agl) (m)
ESP	Estevan Point, British Columbia	49.4° N	126.5° W	7 / 40
LLB	Lac La Biche, Alberta	55.0° N	112.5° W	548 / 50
ETL	East Trout Lake, Saskatchewan	54.4° N	105.0° W	500 / 105
CHC	Churchill, Manitoba	58.7° N	93.8° W	16 / 60
FRA	Fraserdale, Ontario	49.8° N	81.5° W	210 / 40
EGB	Egbert, Ontario	44.2° N	79.8° W	225 / 25
SBL	Sable Island, Nova Scotia	43.9° N	60.0° W	2 / 25
CHM ^{*†}	Chibougamau, Quebec	49.7° N	74.3° W	383 / 30
CHA ^{*†}	Chapais, Quebec	49.8° N	75.0° W	381 / 30

147 ^{*}Chibougamau, Quebec is replaced by Chapais, Quebec ~50 km away from 2011 to 2015, overlapping in Fig.1

148 [†] Site is used to evaluate the posterior inversion results, and is not used in the inversion itself

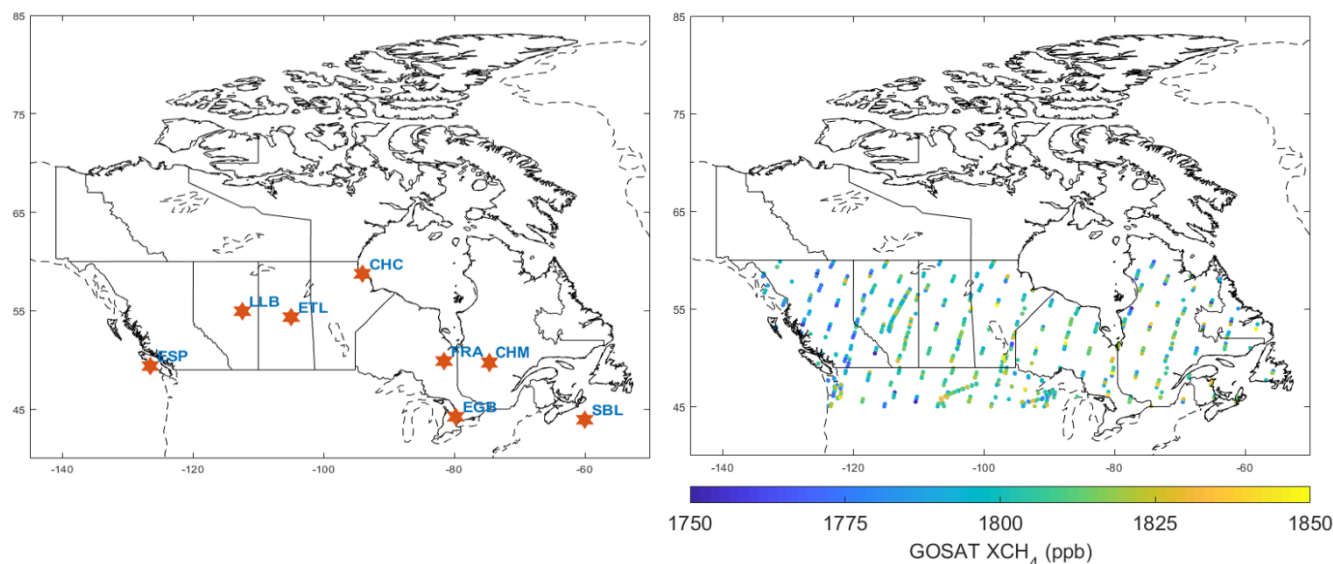
149

150 2.1.2 GOSAT Satellite Observations

151 The Greenhouse Gas Observing Satellite (GOSAT) was launched in January 2009 by the Japan Aerospace Exploration Agency
152 (JAXA). GOSAT is in a low-Earth polar sun-synchronous orbit with an equator overpass around 13:00 local time. The
153 TANSO-FTS instrument on-board GOSAT retrieves column-averaged dry air mol fractions of methane using short-wave



154 infrared (SWIR) solar backscatter in the 1.65 μm absorption band (Butz et al., 2011). Observation pixels in the default mode
155 are 10 km in diameter separated by 260 km along the orbit track with repeated observations every 3 days. Target mode
156 observations provide denser spatial coverage over areas of interest. There has been no observed degradation of GOSAT data
157 quality since the beginning of data collection (Kuze et al., 2016). Here we use version 7 of the University of Leicester proxy
158 methane retrieval over land from January 2010 to December 2015 (Parker et al., 2011, 2015; ESA CCI GHG project team,
159 2018). The single-observation precision of GOSAT XCH₄ data is 13 ppb, and the relative bias is 2 ppb when validated against
160 the Total Column Carbon Observing Network (TCCON; Buchwitz et al., 2015). Figure 1 shows the GOSAT observations over
161 Canada used in our analysis within the domain of 45° N–60° N latitude and 50° W–150° W longitude. The observations used
162 have passed all quality assurance flags for a total of 45,936 observations from 2010–2015, or approximately ~7600
163 observations per year. Our analysis excludes glint data over oceans, and cloudy conditions are accounted for by the quality
164 assurance flags. We avoid using data above 60° N latitude due to higher uncertainty in the satellite retrieval and the model
165 comparison (Maasakkers et al., 2019; Turner et al., 2015).
166



167
168 **Figure 1:** ECCC surface (left) and GOSAT satellite (right) observations used in the inverse analysis. A descriptive list of the
169 ECCC sites is shown in Table 1. GOSAT data shown is from a single year in 2013 and is filtered to the Canadian domain
170 within 45°N–60°N latitude and 50°W–150°W longitude. There are ~600 GOSAT observations per month in this domain with
171 a minimum Nov–Jan (112–248) and maximum Jul–Sep (872–1098), individual months are shown in the Supplement (Fig. S1).
172



173 2.2 Forward Model

174 We use the GEOS-Chem CTM v12-03 at $2^\circ \times 2.5^\circ$ grid resolution driven by 2009–2015 MERRA-2 meteorological fields from
175 the NASA Global Modeling and Assimilation Office (GMAO). Initial conditions from January 2009 are from a previous
176 GOSAT inversion by Turner et al. (2015) which was shown to be unbiased globally when compared to surface and aircraft
177 data. Bottom-up anthropogenic emissions in GEOS-Chem are from the 2013 ICF Canadian oil and gas inventory (Sheng et
178 al., 2017) and the 2012 EDGAR v4.3.2 global inventory for other Canadian and global sources, and the gridded US 2012 EPA
179 Inventory for the United States (Maasakkers et al., 2016). For wetlands, six configurations from the 2010–2015 extended
180 ensemble of WetCHARTS (Bloom et al., 2017) are used in the ensemble forward model analysis (Section 3.2) and the
181 ensemble mean is used as the prior for the inverse analysis (Sections 3.3–3.4). Figure 2 shows the spatial distribution of the
182 prior methane emissions in Canada from the major anthropogenic and natural sources. The two largest sources are from the
183 ICF oil and gas inventory, (Sheng et al., 2017) and wetlands emissions from the ensemble mean of the WetCHARTS inventory
184 (Bloom et al., 2017), with significant emissions from livestock and waste emissions from EDGAR. Oil and gas are 54% of the
185 anthropogenic total and wetlands are 94% of the natural total. The prior emissions estimates in this simulation are summarized
186 in Table 2, which organizes emissions by Canadian source categories and are compared to sector attribution in the National
187 GHG Inventory (Environment and Climate Change Canada, 2017). Our totals for Energy, Agriculture and Waste are 2.4, 1.0,
188 and 0.9 Tg a^{-1} respectively compared to 2.0, 1.2 and 0.9 Tg a^{-1} in the National Inventory. In the absence of a spatially
189 disaggregated Canadian inventory for methane, we consider these prior estimates reasonably similar for the purpose of
190 comparing our posterior emissions to the National Inventory, however we cannot compare the spatial pattern of emissions
191 which may show less agreement. Emissions from the United States and the rest of the world are included in the model but not
192 optimized in the inversions. Loss of methane from oxidation due to OH is computed using archived 3-D monthly fields of OH
193 from a previous GEOS-Chem full-chemistry simulation (Wecht et al., 2014).

194
195
196
197
198
199
200
201
202
203
204
205



206

207 **Table 2:** Mean 2010–2015 prior estimates of Canadian methane emissions used in GEOS-Chem arranged according to
 208 categories in the National GHG Emissions Inventory (Environment and Climate Change Canada, 2017).

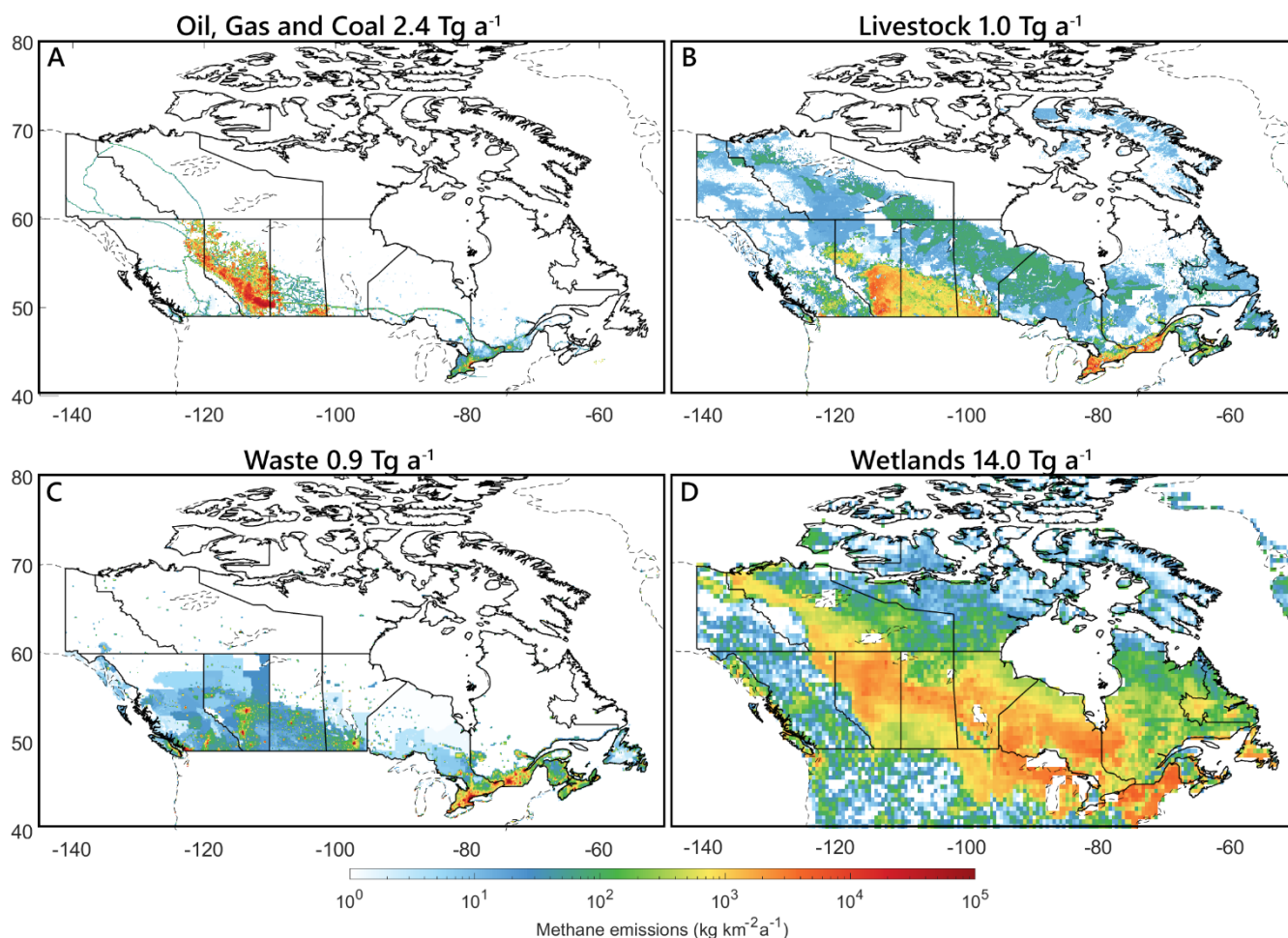
209

Category	Source Type ^a	Emissions (Tg a ⁻¹) ^a	Total (Tg a ⁻¹) ^a	Inventory (Tg a ⁻¹) ^b	
Anthropogenic	Oil	0.52	2.42	2.00	
	Energy Gas	1.81			
	Coal	0.09			
	Agriculture	Livestock	1.00	1.00	1.20
	Waste	Landfills	0.66	0.94	0.92
		Wastewater	0.19		
Other Anthropogenic		0.09			
Wetlands	-	14.0	14.0	-	
Natural	Other Biomass Burning	0.28	0.84	-	
	Seeps	0.28			
	Natural Termites	0.28			

210 ^aEmissions inputs for GEOS-Chem. These are shown for the individual source types and summed over the categories
 211 Energy, Agriculture and Waste. In Canada, oil and gas are from Sheng et al. (2017), coal, livestock, landfills, wastewater and
 212 other anthropogenic are from EDGAR v4.3.2, wetlands are from Bloom et al. (2017). Biomass burning is from QFED
 213 (Darmenov and da Silva, 2013) and termite emissions are from Fung et al. (1991). Seeps and other global sources are
 214 described in Maasakkers et al. (2019).

215

216 ^bEmissions from the National GHG Emissions Inventory (Environment and Climate Change Canada, 2017) that correspond
 217 to the Energy, Agriculture and Waste categories. These are used in the discussion of results but are not included in the
 218 inverse model.



219

220 **Figure 2:** Prior estimates of anthropogenic and natural methane emissions. Colour bars are in log scale in units of kg CH_4
221 $\text{km}^{-2} \text{a}^{-1}$. Most anthropogenic emissions fall under the energy category (A) which are oil and gas in the ICF inventory (Sheng
222 et al., 2017) plus minor emissions from coal in EDGAR 4.3.2. Livestock (B) and waste (C) are from EDGAR. Natural
223 emissions are primarily wetlands from the WetCHARTS inventory (D; Bloom et al., 2017).

224 2.3 Inverse Model Methodology

225 We optimize emissions in the inverse analysis by minimizing the Bayesian cost function $J(\mathbf{x})$ (Rodgers, 2000).

226

$$227 J(\mathbf{x}) = \frac{1}{2} (\mathbf{x} - \mathbf{x}_a)^T \mathbf{S}_a^{-1} (\mathbf{x} - \mathbf{x}_a) + \frac{1}{2} (\mathbf{y} - F(\mathbf{x}))^T \mathbf{S}_o^{-1} (\mathbf{y} - F(\mathbf{x})) \quad (1)$$

228

229 Where \mathbf{x} is the vector of emissions being optimized, \mathbf{x}_a is the vector of prior emissions (Table 2), $F(\mathbf{x})$ is the simulation of
230 methane concentrations corresponding to the observation vector \mathbf{y} of ECCC surface and/or GOSAT data. \mathbf{S}_a is the prior error



231 covariance matrix and \mathbf{S}_o is the observational error covariance matrix. The observational error matrix includes both instrument
232 and model transport error. The GEOS-Chem model relating methane concentrations to emissions $F(\mathbf{x})$ is essentially linear and
233 can be represented by the Jacobian matrix \mathbf{K} such that $F(\mathbf{x}) = \mathbf{K}\mathbf{x} + \mathbf{b}$, where \mathbf{b} is the model background. The background
234 includes initial conditions from Turner et al. (2015) and methane from global emissions that are held constant in the inversion.
235 Possible bias in the background is evaluated in detail in Section 3.1 and shown to be minimal. The \mathbf{K} matrix is of n by m size
236 where n is the number of state vector elements being optimized and m is the number of ECCC surface and/or GOSAT
237 observations being used. The \mathbf{K} matrix is constructed using the forward mode of GEOS-Chem and the tagged tracer output for
238 Canadian sources which describes the sensitivity of concentrations to emissions dy/dx in ppb Tg^{-1} .

239

240 GEOS-Chem continuously simulates global emissions with a global source-sink imbalance of $+13 \text{ Tg a}^{-1}$ in the budget as
241 described in Maasakkers et al. (2019). We show in Section 3.1 that this configuration of the model reliably reproduces the
242 global growth rate in atmospheric methane with adjustments only needed for 2014 and 2015 primarily due to differences in
243 tropical wetland emissions (Maasakkers et al., 2019). A high resolution inversion over North America over the 2010–2015
244 time-period using the same prior has shown adjustments to US emissions near the Canadian border are also relatively minimal,
245 (Maasakkers et al., 2020), so we treat US emissions as constant. This gives a well-represented background for methane which
246 is checked using global GOSAT data and in situ data at Canadian background site ESP. Hence, we can attribute the model-
247 observation mismatch ($\mathbf{y} - F(\mathbf{x})$) using observations limited to Canada to Canadian emissions which are optimized in the
248 inversion. Here we show three inversions with a different number of state vector elements: a) the monthly inversion ($n = 78$)
249 optimizes monthly natural emissions in Canada and yearly anthropogenic emissions from 2010–2015, b) the sectoral inversion
250 ($n = 5$) optimizes emissions according to the major inventory categories in Table 2 done individually for each year, and c) the
251 provincial inversion ($n = 16$) optimizes emissions according to subnational boundaries which is also repeated for each year.
252 The monthly inversion provides high temporal resolution to constrain the seasonality of natural emissions, assuming the spatial
253 distribution is correct. The sectoral inversion provides direct constraints on inventory categories, and the provincial inversion
254 provides higher spatial resolution for subnational attribution. Substituting $F(\mathbf{x}) = \mathbf{K}\mathbf{x}$ in eq. 1 and subtracting the background
255 \mathbf{b} , the analytical solution of the cost function $dJ(\mathbf{x})/d\mathbf{x} = 0$ yields the optimal posterior solution $\hat{\mathbf{x}}$ (Rogers, 2000):

256

$$257 \hat{\mathbf{x}} = \mathbf{x}_a + \mathbf{S}_a \mathbf{K}^T (\mathbf{K} \mathbf{S}_a \mathbf{K}^T + \mathbf{S}_o)^{-1} (\mathbf{y} - \mathbf{K} \mathbf{x}_a) \quad (2)$$

258

259 The analytical solution provides closed-form error characterization, the posterior error covariance $\hat{\mathbf{S}}$ of the posterior solution
260 $\hat{\mathbf{x}}$ is given by:

261

$$262 \hat{\mathbf{S}} = (\mathbf{K}^T \mathbf{S}_o^{-1} \mathbf{K} + \mathbf{S}_a^{-1})^{-1} \quad (3)$$

263

264 The averaging kernel matrix \mathbf{A} is used to evaluate the surface and satellite observing systems and is given by:



265

$$266 \quad \mathbf{A} = \mathbf{I}_n - \hat{\mathbf{S}}\mathbf{S}_a^{-1} \quad (4)$$

267

268 where \mathbf{I}_n is the identity matrix of length n corresponding to the number of state vector elements. The averaging kernel matrix
269 \mathbf{A} describes the sensitivity of the posterior solution $\hat{\mathbf{x}}$ to the true state \mathbf{x} ($\mathbf{A} = d\hat{\mathbf{x}}/d\mathbf{x}$). The trace of \mathbf{A} provides the degrees of
270 freedom for signal (DOFS), which is the number of pieces of information of the state vector that is gained from the inversion
271 (DOFS $\leq n$). The diagonal values of \mathbf{A} provide information on which Canadian state vector elements can be constrained by
272 ECCO surface and GOSAT satellite observations above the noise, and higher DOFS closer to n correspond to better constrained
273 sources in total. As a further diagnostic of the inversion we conduct a singular value decomposition of the prewhitened Jacobian
274 $\check{\mathbf{K}} = \mathbf{S}_o^{-1/2}\mathbf{K}\mathbf{S}_a^{1/2}$ (Rodgers, 2000). The number of singular values greater than one is the effective rank of $\check{\mathbf{K}}$, which shows the
275 independence of the state vector elements and the number of pieces of information above the noise that are resolved in the
276 inversion (Heald et al., 2004). The comparison between this eigenanalysis and the DOFS are discussed in the Supplement and
277 is used to inform the limitations of the observation system.

278

279 We construct the prior error covariance matrix \mathbf{S}_a based on aggregated error estimates for source categories and regions. We
280 use 50% error standard deviation for the aggregated anthropogenic emissions which includes the Sheng et al. (2017) oil and
281 gas inventory other EDGAR sources, 60% for wetlands emissions from the Bloom et al. (2017) WetCHARTS inventory and
282 100% for non-wetlands natural sources. We assume no correlation between state vector elements so that \mathbf{S}_a is diagonal.
283 Anthropogenic emissions have been shown to be spatially uncorrelated (Maasakkers et al., 2016) however wetlands show
284 spatial correlation (Bloom et al., 2017). Here we optimize broadly aggregated categories, so our method assumes the spatial
285 pattern of each state vector element is correct, however correlations between state vector elements in the eigenanalysis are
286 used to assess the limitations of source discretization in the observing systems.

287

288 We construct the diagonal observation error matrix \mathbf{S}_o which captures instrument and model error using the relative residual
289 error method (Heald et al., 2004). In this approach the vector of observed-modelled differences $\Delta = y_{\text{GEOS-Chem}} - y_{\text{observations}}$ is
290 calculated and the mean observed-modelled difference $\overline{\Delta} = \overline{y_{\text{GEOS-Chem}} - y_{\text{observations}}}$ is attributed to the emissions that will
291 be optimized. Hence, the standard deviation in the residual error $\Delta' = \Delta - \overline{\Delta}$ represents the observational error and is used as
292 the diagonal elements of \mathbf{S}_o . For our Canadian inversion we find positive model-observation biases in the warmer months
293 (April to September) and negative biases in the colder months (October to March). We calculate the relative residual error for
294 growing and non-growing seasons separately, such that Δ' is partitioned into Δ'_g (October to March) and Δ'_{ng} (April to
295 September) which is then used to calculate the diagonal elements of \mathbf{S}_o . For surface observations the mean observational error
296 is 65 ppb. Since the instrument error is <1 ppb for afternoon mean methane measurements, the observational error is entirely
297 attributed to transport and representation error of surface methane in the model grid pixels. For satellite observations the mean



298 observational error is 16 ppb where the instrument error is 11 ppb, showing most of the observational error is from the
299 instrument rather than the forward model representation of the total column. Column-averaged methane concentrations are
300 less sensitive to surface emissions resulting in the lower model error (Lu et al., 2020).

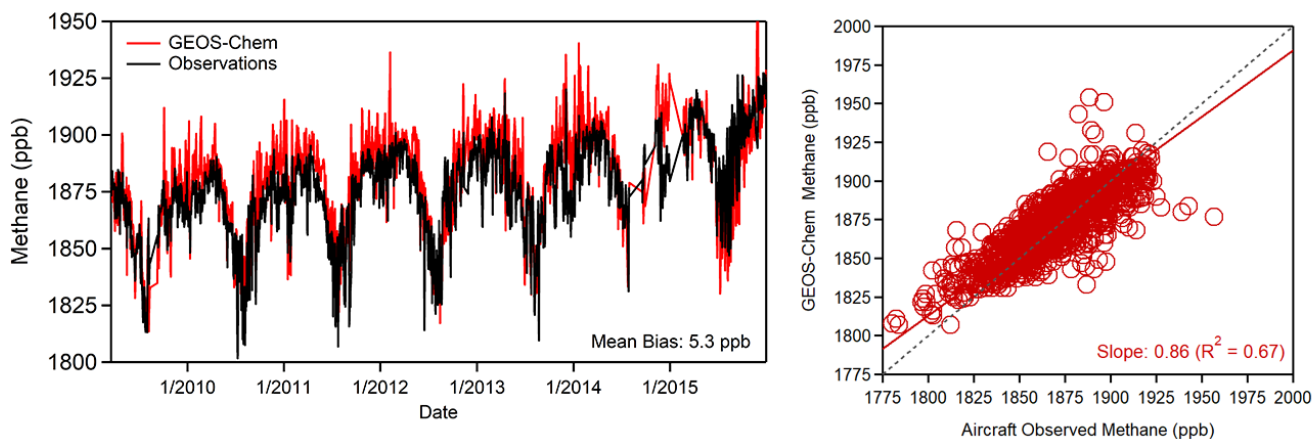
301 **3 Results and Discussion**

302 **3.1 Evaluation of Bias in the Global Model**

303 The left panel of Figure 3 shows the comparison of monthly mean GEOS-Chem surface methane concentrations and methane
304 measured at the ECCC station ESP from 2009 to 2015. ESP is located at the west coast of Vancouver Island (Fig. 1); this site
305 is used as an evaluation of background methane and tests the bias in the global model as it is the least sensitive to Canadian
306 emissions due to westerly prevailing winds. The model reliably reproduces surface observations at this station and the growth
307 rate in background methane due to the source-sink imbalance of $+13 \text{ Tg a}^{-1}$ in the model global budget (Maasakkers et al.,
308 2019) with a small mean model-observation bias of 5.3 ppb. The right panel of Figure 3 shows the comparison of modelled
309 methane to NOAA aircraft profiles at the same site. Aircraft profiles occur approximately once a month continuously over the
310 study period. The data is not averaged here and is directly compared to GEOS-Chem simulated grid boxes at the pressure level
311 of the measurement. The reduced mean axis (RMA) regression shows a slope of 0.86 and a coefficient of regression $r^2 = 0.67$
312 which shows a reasonable model representation of the measurements. These statistics are consistent with previous inversions
313 using GEOS-Chem that showed relatively unbiased conditions against NOAA surface stations globally (Turner et al., 2015;
314 Maasakkers et al., 2019). A high resolution inversion over North America over the same 2010–2015 time-period using the
315 same prior have shown adjustments to US emissions near the Canadian border are relatively minimal (Maasakkers et al., 2020),
316 so we treat US emissions as constant in the inversion. The acceptable reproducibility of background methane at this site allows
317 us to attribute much larger differences observed at other sites, up to a maximum of ~ 1000 ppb in the summer (Figure 6), to
318 Canadian emissions which are optimized using Canadian observations while holding other global emissions constant.

319

320



321
322

323 **Figure 3:** Time-series comparison (left) from 2009–2015 of surface GEOS-Chem simulated methane (red) and measured in
324 situ methane (black) at site ESP off the west coast of British Columbia. Comparison to NOAA aircraft profiles (right) from
325 2009–2015 at the same site using a reduced major axis (RMA) regression along with the 1:1 line (black).

326

327 The GEOS-Chem simulation of column averaged methane shows three global biases previously discussed in the literature: (1)
328 a latitude-dependent bias, (2) a seasonal bias and (3) a background change for 2014 and 2015 due to differences in the global
329 source-sink imbalance in these two years (Turner et al., 2015; Saad et al., 2018; Maasakkers et al., 2019; Stanevich et al.,
330 2019). We apply these corrections to the simulated column of methane on a global basis to produce an unbiased background
331 for our target Canadian domain (45° N to 60° N, 50° W to 150° W). The latitude-dependent bias (1) is likely due to excessive
332 polar stratospheric transport (Stanevich et al., 2019). We correct for this bias by fitting the model-GOSAT difference for global
333 2° × 2.5° grid cells according to a second-order polynomial as shown in Figure 4:

334

$$\xi = (2.2\theta^2 - 34\theta) \times 10^{-3} - 2.7$$

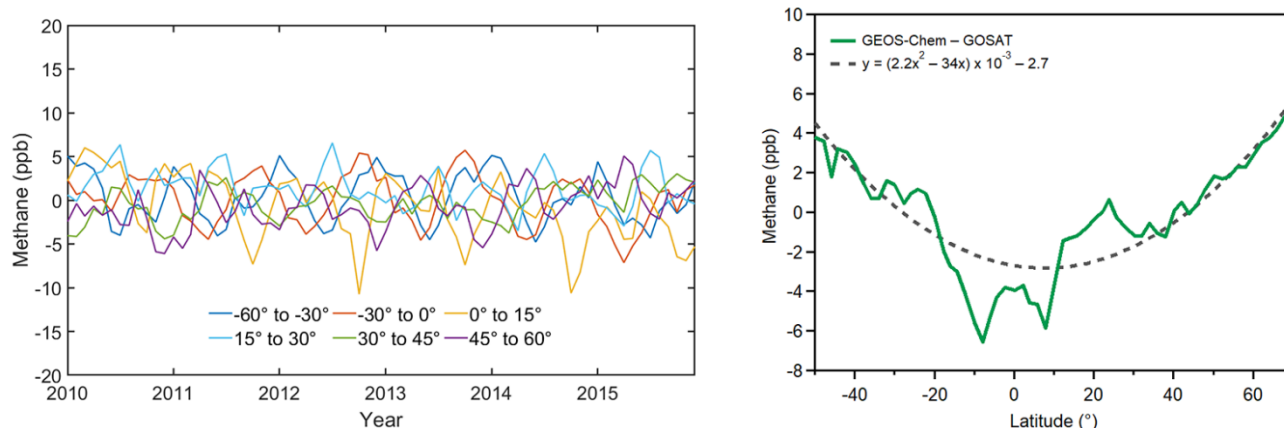
(5)

336

337 where ξ is the resulting bias correction in ppb and θ is latitude in degrees. The correction in this work for the latitude bins of
338 our target domain (45° N to 60° N) is between 0.3 to 2.9 ppb. This correction is lower than what has been shown previously
339 (Turner et al., 2015; Maasakkers et al., 2019) and we attribute this improvement to our use of a 2°x2.5° gridded simulation
340 instead of a 4°x4.5° as recommended by Stanevich et al. (2019) to reduce transport errors. A seasonally oscillating bias (2)
341 remains after this correction. The seasonal bias has an amplitude of ± 4 ppb with repeating maxima in June and minima in
342 December. It is not clear whether this seasonal bias is due to emissions and/or transport errors. In our base case we remove the
343 seasonal bias on a monthly basis following Maasakkers et al. (2019) and show a sensitivity test without the correction for our
344 inversion of monthly natural emissions in Canada (Supplement 1.3). Inversion results using GOSAT data with and without
345 bias corrections in the model simulation of total column methane do not show major differences (Fig. S3). These scenarios all



346 show agreement with the posterior emissions adjustments determined using ECCC in situ data – which is a useful benchmark
347 since modelled methane at the surface is not subject to any bias corrections. The background change (3) that appears in the
348 simulated methane column from 2014 onwards is corrected for in Maasackers et al. (2019) by optimizing emissions, emissions
349 trends and trends in OH using a global inversion. In that work correction factors do not appear over Canada and the United
350 States that would significantly influence the global change in atmospheric methane, and the main adjustment in 2014 and 2015
351 were to tropical wetlands emissions and OH. Here we treat this as a background change and apply a uniform correction to the
352 simulated column since emissions outside of Canada and changes in OH are treated as fixed in our Canada-focused inversion.
353 The background change (3) is 5 ppb in 2014 and 10 ppb in 2015. The right panel of Figure 4 shows the latitude dependent bias
354 correction and the left panel shows the resulting global time-series of GEOS-Chem total column methane from 2010–2015
355 after corrections are applied. The global GEOS-Chem – GOSAT differences in the methane column can be limited globally to
356 within 10 ppb without including the seasonal bias correction, and within 5 ppb with its inclusion. This shows a steady
357 background in methane for the entire time period from 2010–2015 so global emissions do not affect the optimization of
358 Canadian emissions. While biases within 10 ppb have been treated as acceptable for methane inversions (Buchwitz et al.,
359 2015), we evaluate our GOSAT inversion results against inversions with independent ECCC in situ measurements that do not
360 require any bias corrections in the model (Section 3.3) to produce more robust emissions estimates.
361



362
363

364 **Figure 4:** Time series (left) from 2010–2015 of the difference between GEOS-Chem simulated total column methane and
365 GOSAT observations after applying bias corrections, showing a consistent global background for methane. Data used in the
366 inversion for Canada is from 45° N to 60° N (purple line) and shows acceptable differences within 5 ppb over the entire
367 global latitude band. To produce the left figure, the latitude-dependent bias (right) is shown with the polynomial correction
368 that is applied (gray dash) that is within a magnitude of 0.3 to 2.9 ppb for the same latitude.

369



370 **3.2 Evaluation of WetCHARTS Extended Ensemble for Wetlands Emissions in Canada**

371 Wetlands are the largest methane source in Canada with uncertainties in the magnitude, seasonality, and spatial distribution of
372 emissions. Our inverse analysis constrains the magnitude and seasonality of emissions with observations. Ideally, the prior
373 emissions in the model should be the best possible representation of emissions to reduce error in the optimization problem
374 (Jacob et al., 2016). Table 2 shows 2010–2015 mean wetlands emissions in Canada to be 14.0 Tg a^{-1} from the mean of the
375 WetCHARTS v1.0 inventory (Bloom et al., 2017). These emissions are more than three times the total of anthropogenic
376 emissions 4.4 Tg a^{-1} . The much larger signal from wetlands emissions poses a difficulty for constraining anthropogenic
377 emissions (Miller et al., 2014). In this section, we evaluate our use of the mean of the WetCHARTS v1.0 extended ensemble
378 by running a series of forward model runs using alternate ensemble members in GEOS-Chem and comparing model output to
379 ECCC in situ observations.

380

381 The WetCHARTS extended ensemble for 2010–2015 contains an uncertainty dataset of 18 possible global wetlands
382 configurations as described in Bloom et al. (2017). These depend on three processing parameters which are: three $\text{CH}_4\text{:C}$
383 temperature-dependent respiration fractions ($q_{10} = 1, 2, \text{ and } 3$; where 1 is the highest temperature dependency), two inundation
384 extent models (GLWD vs. GLOBCOVER; where GLWD corresponds to higher inundation in Canada) and three global scaling
385 factors for global emissions to amount to 124.5, 166 or $207.5 \text{ Tg CH}_4 \text{ yr}^{-1}$ ($3 \times 2 \times 3 = 18$). We find using the scaling factors
386 corresponding to 124.5 and $207.5 \text{ Tg CH}_4 \text{ yr}^{-1}$ within GEOS-Chem results in an imbalance in the global budget beyond what
387 is observed in our measurements and degrades the representation of background methane, so we limit the extended ensemble
388 to six members which depend on three temperature parameterizations and two inundation scenarios ($3 \times 2 = 6$). Figure 5 shows
389 the magnitude and spatial distribution of wetlands emissions in the six scenarios. The total wetlands emissions within Canada
390 show nearly an order of magnitude difference between ensemble members from 3.9 Tg a^{-1} to 32.4 Tg a^{-1} . Compared to the rest
391 of North America, Boreal Canada shows the largest variability between ensemble members, with the Southeast United States
392 as the second most uncertain (Sheng et al., 2018b).

393

394 We use ECCC in situ observations to better constrain the range of wetlands methane emissions in the ensemble members. All
395 six configurations are used in GEOS-Chem to produce a series of forward model runs for a subrange of years between 2013–
396 2015. Figure 6 shows GEOS-Chem simulated methane concentrations using the six WetCHARTS configurations and compares
397 to four ECCC in situ measurement sites in Canada (LLB, ETL, FRA, EGB). This subset of available data is representative of
398 sites sensitive to both anthropogenic and natural emissions. Most of Canadian anthropogenic emissions are from Western
399 Canada (Fig. 2), which we use sites LLB and ETL to evaluate (Fig. 1), and a significant amount of Canadian natural emissions
400 are from region surrounding the Hudson's Bay Lowlands, which we use sites FRA and EGB to evaluate. Methane
401 concentrations from GEOS-Chem show large differences when compared to ECCC observations, ranging from +1050 to –150
402 ppb. The boundary-condition site ESP (Fig. 3) showed a mean bias of 5.3 ppb for all of 2010–2015. Since there is no similar



403 mismatch in the global representation of methane, these biases up to 1050 ppb can therefore be attributed to misrepresented
404 local Canadian emissions plus associated transport and representation error. Two types of biases with opposite signs appear
405 from this comparison. The first type is a positive summertime bias where the modelled methane concentrations significantly
406 exceed the observations; this bias is more pronounced in sites FRA (Fig. 6-C) and EGB (Fig. 6-D), which are in Ontario and
407 sensitive to the Hudson Bay Lowlands. The bias is also visible in the western sites LLB (Fig. 6-A) and ETL (Fig. 6-B) to a
408 lesser extent. As we use a smaller magnitude of wetlands methane emissions corresponding to the ensemble members in Figure
409 5 (from 32.4 Tg a⁻¹ to 3.9 Tg a⁻¹), this summertime bias decreases proportionately. Therefore, we can attribute these large
410 positive summertime biases to growing season wetlands emissions that are overestimated in the process model configurations.
411 The second type of bias is a year-long negative bias that appears most in site LLB (Fig. 6-A) and is magnified with the use of
412 lower-magnitude wetlands emissions. This suggests the presence of year-round anthropogenic emissions in Western Canada
413 that are underestimated in the prior, or that winter-time wetland emissions could also be underestimated in WetCHARTS due
414 to the lack of explicit soil water and temperature dependencies. The inverse modelling results in the next section attribute this
415 bias to anthropogenic emissions.

416

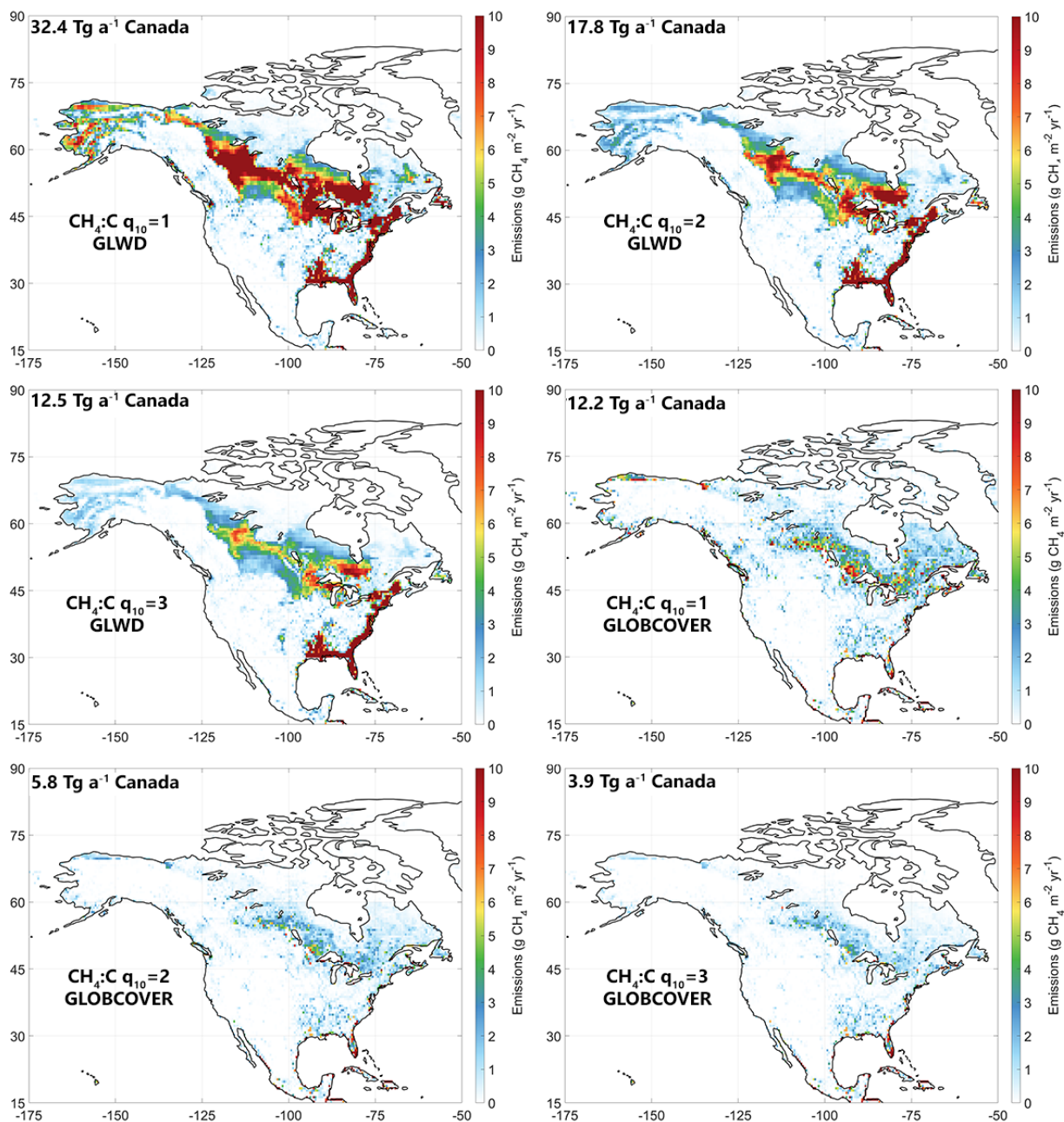
417 Miller et al. (2016) conducted a study constraining North American Boreal wetlands emissions from the WETCHIMP
418 inventory modelled in WRF-STILT by comparing to observations in 2008. Their study included the use of three of the ECCC
419 stations described here (CHM, FRA and ETL). The model comparison to observations in that study showed a similar pattern
420 of modelled methane exceeding observations in the summer and a low bias at ETL. They suggested wetlands emissions were
421 overestimated in most model configurations and that the wetlands bias may be masking underestimated anthropogenic
422 emissions. These conclusions are corroborated by the 2013–2015 comparison shown here, we show high wetlands emissions
423 configurations in WetCHARTS produce a high bias that exceed measured summertime methane concentrations, and the use
424 of lower wetlands configurations reveal a year-long low bias apparent in Western Canada. Our results suggest the combined
425 use of higher inundation extent and lower temperature dependencies (GLWD and $q_{10} = 3$), or the use of lower inundation
426 extent and higher temperature dependencies (GLOBCOVER and $q_{10} = 1$) best reproduce observations near the mean of the
427 range of emissions, although the ensemble forward model analysis is unable to specify more detailed process model constraints.

428

429 The forward model analysis in this section is a direct evaluation of wetlands configurations. This approach allows us *manually*
430 tune wetlands scenarios and diagnose the sensitivity of the modelled-observed differences to the process modelling parameters.
431 The inverse analysis shown subsequently is a statistical optimization that applies scaling factors to emissions based on the
432 same model-observation differences. The inverse analysis can be viewed analogously as an *automatic* approach. These results
433 show the challenge with optimizing Canadian methane emissions when wetlands emissions are largely uncertain. Our approach
434 of optimizing anthropogenic and natural emissions simultaneously in an inversion is useful because attempting to constrain
435 either emissions category, anthropogenic or natural, obfuscates the analysis on the other. We exploit the different pattern of
436 anthropogenic and natural emissions in time and space (Fig. 6). Natural emissions peak in the summertime and are concentrated



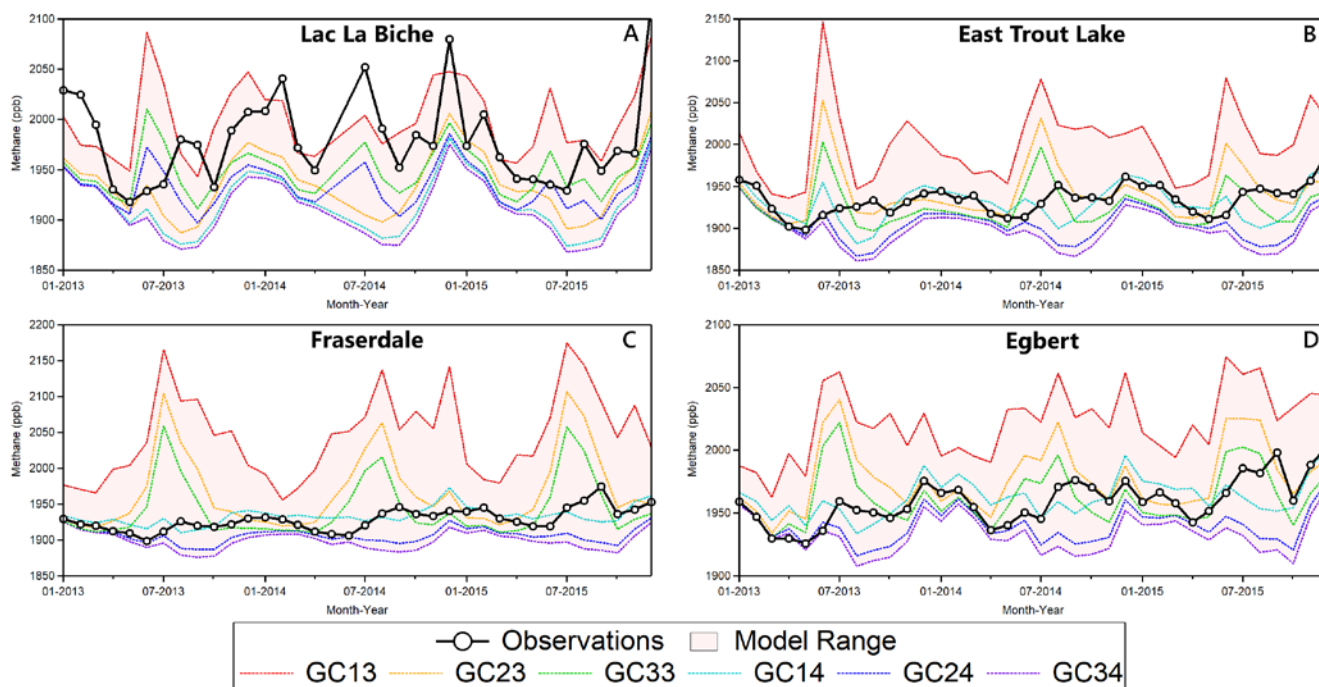
437 in Boreal Canada, while anthropogenic emissions are persistent year-round and are concentrated in Western Canada (Fig. 2).
438 Hence when optimizing the model-observation mismatch in a Bayesian inverse framework, some elements of the observation
439 vector will correspond to high biases from summertime observations in Boreal Canada and some elements will correspond to
440 low biases in Western Canada. As the choice of prior for the inversion we use the mean of the WetCHARTS configurations
441 (14.0 Tg a^{-1}) which corresponds to the middle of the range shown shaded in red in Figure 6. The 60% range of uncertainty in
442 the prior error covariance matrix \mathbf{S}_a appropriately excludes the extreme scenarios in Fig. 5 and 6.
443



444

445

446 **Figure 5:** Ensemble members from the WetCHARTS v1.0 inventory (Bloom et al., 2017) with totals for wetland methane
447 emissions within Canada for each configuration shown in Tg CH₄ a⁻¹. Ensemble members vary according to the use of three
448 CH₄:C q₁₀ temperature dependencies and two inundation extent scenarios (GLWD vs. GLOBCOVER) for 3×2=6 scenarios.



449

450 **Figure 6:** Time series of 2013–2015 modelled and observed methane concentrations. Monthly-mean methane from ECCC in
451 situ observations (black) are shown and compared to six GEOS-Chem simulations differing in the use of WetCHARTS
452 ensemble members for wetlands emissions. The six configurations are labelled GCXY where first digit ($X=1,2,3$) corresponds
453 to the $\text{CH}_4:\text{C}$ q_{10} temperature dependency, which decreases the sensitivity of emissions to temperature with increasing value.
454 The second digit ($Y=3,4$) corresponds to the model used for inundation extent (3 = GLWD, 4 = GLOBCOVER) where
455 GLOBCOVER produces lower emissions in Canada. Emissions configurations are those shown in Fig. 5 in order of magnitude
456 from red to purple lines, with the shaded red showing the range of concentrations. Sites are LLB, Alberta (A), ETL,
457 Saskatchewan (B), FRA, Northern Ontario (C) and EGB, Southern Ontario (D).

458

459

460

461

462

463

464

465

466

467



468 3.3 Comparative analysis of inversions using ECCC in situ and GOSAT satellite data

469 We optimize 2010–2015 emissions in Canada using an $n = 78$ state vector element inversion setup with GOSAT and ECCC
470 data independently. Elements 1–72 of the inversion are monthly total natural emissions (wetlands + other natural) from 2010–
471 2015 and elements 73–78 are yearly total anthropogenic emissions (energy + agriculture + waste) for the same years. These
472 categories correspond to the emissions shown in Table 2. We do not optimize emissions according to clustered grid boxes like
473 other satellite inversions using GEOS-Chem (Wecht et al., 2014; Turner et al., 2015; Maasakkers et al., 2019) and instead
474 scale the amplitudes of these two aggregated categories. This approach is a trade-off of time for space, giving up finer spatial
475 resolution for finer temporal resolution. This is useful for optimizing Canadian methane emissions since a) anthropogenic
476 emissions are largely concentrated in Western Canada and require less spatial discretization over the entire country and b)
477 natural emissions are the largest source and have an uncertain seasonality – as shown in the previous section – and require
478 finer temporal discretization. The limitations of this method are that natural emissions are very unlikely to be spatially
479 homogenous and vary due to hydrological differences even at the microtopographic level (Bubier et al., 1993). Perfectly
480 resolving Canadian emissions sources in time and space is challenged by the sparsity and precision of the observing system
481 and the model representation of the observations. We show the limitations of the combined ECCC and GOSAT observing
482 system towards resolving subnational emissions in more detail in the subsequent section.

483
484 Figure 7 (top) shows 2010–2015 posterior emissions using this 78 state vector approach with ECCC in situ data (blue) and
485 GOSAT satellite data (green). Error bars are from the diagonal elements of the posterior error covariance matrix $\hat{\mathbf{S}}$. Posterior
486 anthropogenic emissions averaged over the 6 year period are $6.0 \pm 0.4 \text{ Tg a}^{-1}$ (1σ year-to-year variability) using ECCC data
487 and $6.5 \pm 0.7 \text{ Tg a}^{-1}$ using GOSAT data. Posterior estimates are 36% and 48% higher than the prior of 4.4 Tg a^{-1} for ECCC
488 and GOSAT results, respectively. There does not appear to be a significant year-to-year trend above the noise for the
489 anthropogenic emissions optimized by either dataset. The posterior anthropogenic emissions using ECCC and GOSAT data
490 show agreement with each other in each year but 2011, where the GOSAT derived emissions are statistically higher. The error
491 from the diagonal of the posterior error covariance matrix $\hat{\mathbf{S}}$ may be overly optimistic, particularly for GOSAT data. This is
492 due to the observational error covariance matrix \mathbf{S}_o being treated as diagonal when realistically there are correlations between
493 GOSAT observations that are difficult to quantify (Heald et al., 2004). Our results for anthropogenic emissions show agreement
494 with top-down aircraft estimates of methane emissions in Alberta that are higher than bottom-up inventories (Johnson et al.,
495 2017; Baray et al., 2018) and previous satellite inverse-modelling studies over North America that upscale emissions in
496 Western Canada (Turner et al., 2015; Maasakkers et al., 2019; Maasakkers et al., 2020; Lu et al., 2020). We show source
497 attribution through a sectoral and subnational scale analysis of anthropogenic emissions in the subsequent section.

498
499 Inversion results for monthly natural emissions from 2010–2015 are also shown in Figure 7 (bottom). The total of posterior
500 natural emissions averaged over the 6 year period is $10.5 \pm 1.9 \text{ Tg a}^{-1}$ using ECCC data and $11.7 \pm 1.2 \text{ Tg a}^{-1}$ using GOSAT



501 data. The prior for natural emissions is 14.8 Tg a^{-1} from the mean of the WetCHARTS extended ensemble (14.0 Tg a^{-1}) plus
502 other natural (biomass burning + termites + seeps = 0.8 Tg a^{-1}). There is some interannual variability in the prior due to higher
503 emissions in 2010 and 2015. Posterior results averaged over the six years are 29% lower than the prior using ECCC data and
504 21% lower using GOSAT data, with both posterior results showing agreement with each other. These results are within the
505 uncertainty range of the WetCHARTS extended ensemble, and we show the magnitude of emissions from the larger uncertainty
506 dataset (3.9 to 32.4 Tg a^{-1}) can be better constrained with both ECCC and GOSAT observations. While our results show lower
507 natural emissions in all years, a linear fit to the posterior annual emissions using ECCC data shows a trend of increasing natural
508 emissions at a rate of $\sim 1.0 \text{ Tg a}^{-1}$ per year from 2010–2015. The posterior with GOSAT data does not corroborate this result,
509 the overall emissions trend using GOSAT data is not robust and shows a decreasing trend of $\sim 0.2 \text{ Tg a}^{-1}$ per year. The lack of
510 corroboration of trends between ECCC and GOSAT data may be reflective of the lower overall sensitivity of total column
511 methane to these surface fluxes (Sheng et al., 2017; Lu et al., 2020) or the inability of this inverse system to constrain trends
512 sufficiently. Poulter et al. (2017) estimated global wetlands emissions using biogeochemical process models constrained by
513 inundation and wetlands extend data. They estimated mean annual emissions over all of Boreal North America to be $25.1 \pm$
514 11.3 Tg a^{-1} in 2000–2006, $26.1 \pm 11.8 \text{ Tg a}^{-1}$ in 2007–2012 and $27.1 \pm 12.5 \text{ Tg a}^{-1}$ which suggests a small increasing trend.
515 Observational constraints over longer timescales are necessary to investigate the possibility of trends in Canadian natural
516 methane emissions. Improvements to the observation network and a better understanding of climate sensitivity in
517 WetCHARTS are necessary to understand how wetlands methane emissions will evolve in future climates.

518

519 Figure 8 shows the 2010–2015 average seasonal pattern of natural emissions in the prior and posterior results. The seasonality
520 of natural methane emissions in the prior shows a sharp peak in July with a narrow methanogenic growing season. The posterior
521 with ECCC data shows a peak 1-month later in August in most years instead of July, with lower than prior emissions in the
522 spring months before the peak (March to May) and similar emissions to the prior in the autumn months after the peak
523 (September to November). Posterior emissions with GOSAT show a peak in July and corroborates the pattern of slower-to-
524 begin spring emissions and the lower intensity summer peak seen from the ECCC inversion. The posterior results show the
525 seasonality of emissions is not symmetrical around the temperature peak in July. August emissions are higher than June,
526 September emissions are higher than May, and October emissions are higher than April. This pattern around July is present in
527 the prior emissions from WetCHARTS, however the inversion results constrained by ECCC or GOSAT observations intensify
528 the relative difference between emissions before and after July. Miller et al. (2016) found a similar seasonal pattern of
529 emissions in the Hudson Bay Lowlands using an inverse model constrained by 2007–2008 in situ data. They found a less
530 narrow and less intense peak of summertime emissions with higher autumn over spring emissions. Warwick et al. (2016) used
531 a forward model and isotopic measurements of $\delta^{13}\text{C-CH}_4$ and $\delta\text{D-CH}_4$ from 2005–2009 to show northern wetlands emissions
532 should peak in August–September with a later spring kick-off and later autumn decline. This is further corroborated by Arctic
533 methane measurements (Thonat et al., 2017) and high latitude eddy covariance measurements (Peltola et al., 2019; Treat et al.,
534 2018; Zona et al., 2016) that show a larger contribution from the nongrowing season. Our inverse model results using ECCC



535 and GOSAT data both show agreement with slower to start emissions in the spring and a less intense summertime peak for
536 Canadian wetlands emissions.

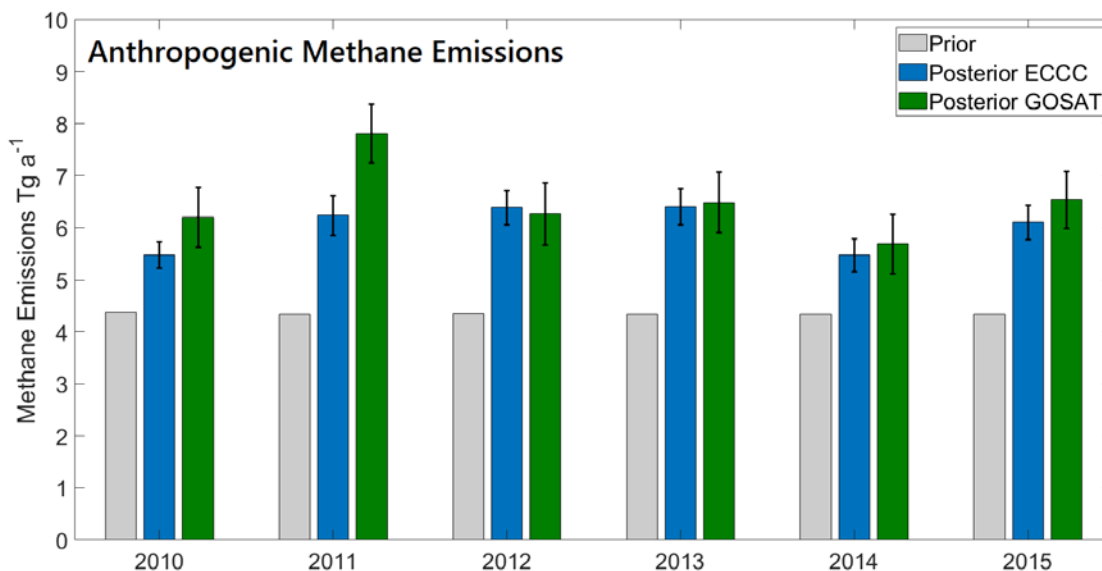
537

538 Several mechanisms have been proposed to describe a larger relative contribution from cold season methane emissions.
539 Pickett-Heaps et al. (2011) attributed a delayed spring onset in the HBL to the suppression of emissions by snow cover. The
540 temperature dependency in WetCHARTS is based on surface skin temperature (Bloom et al., 2017), however subsurface soil
541 temperatures may continue to sustain methane emissions while the surface is below freezing. When subsurface soil
542 temperatures are near 0°C, this “zero curtain” period can further continue to release methane for an extended period (Zona et
543 al., 2016). Subsurface soils may remain unfrozen at a depth of 40 cm even until December (Miller et al., 2016). Alternatively,
544 field studies in the 1990’s suggested the seasonality of emissions may be more influenced by hydrology than temperature, with
545 large differences between peatlands sites (Moore et al., 1994). The WetCHARTS extended ensemble inundation extent variable
546 is constrained seasonally by precipitation. While this does not directly constrain water table depth and wetland extent it
547 provides an aggregate constraint on hydrological variability (Bloom et al., 2017). We show the mean seasonal pattern of both
548 air temperature and precipitation from climatological measurements in subarctic Canada are similarly asymmetrical about the
549 July peak (Fig. S2 in the Supplement). August is warmer and wetter than June, September is warmer and wetter than May, and
550 October is wetter and warmer than April – with wetness being more persistent into the autumn than air temperature. Our
551 inversion results showing a delayed spring start in the seasonal pattern of natural methane emissions in Canada may suggest a
552 lag in the response of methane emissions to temperature and precipitation. This may be due to lingering subsurface soil
553 temperatures and/or more complex parametrization necessary for hydrology.

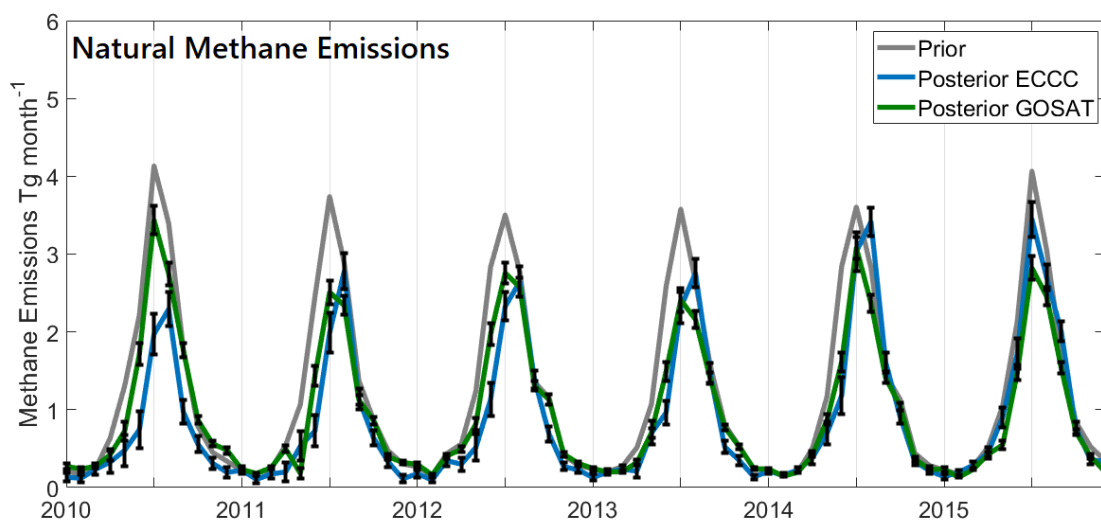
554

555 The overall agreement between ECCC and GOSAT inversions shows robustness in the results. While the same model, prior
556 emissions and inversion procedure are used for assimilating ECCC and GOSAT data, the two datasets are produced with very
557 different measurement methodologies (in situ vs. remote sensing) and sample different parts of the atmosphere (surface
558 concentrations or the total vertical column). The posterior error intervals shown from \hat{S} reflect assumptions about the treatment
559 of observations and may insufficiently account for correlations, however the comparative analysis provides a useful sensitivity
560 test of the posterior emissions since the datasets reflect different treatment of these assumptions.

561



562



563

564 **Figure 7:** Comparative analysis of inversion results optimizing annual total Canadian anthropogenic emissions (top) and
565 monthly total natural emissions (bottom) in an $n = 78$ state-vector element setup. The posterior emissions determined using
566 ECCC in situ (blue) and GOSAT satellite (green) data are compared to the prior (gray). Error bars are from the diagonal
567 elements of the posterior error covariance matrix.

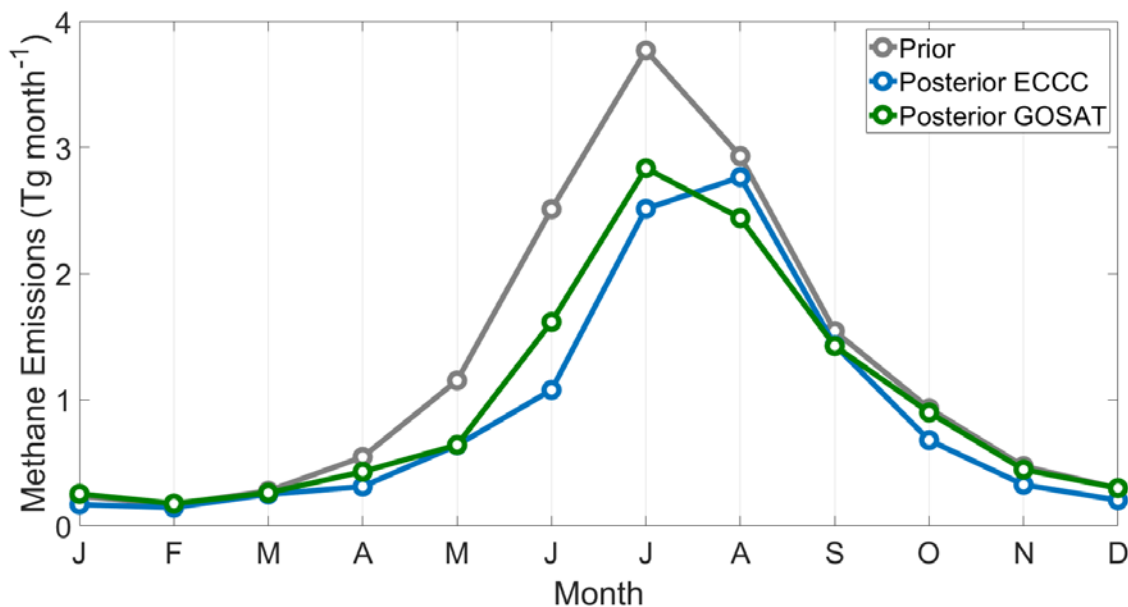
568

569

570



571



572

573 **Figure 8:** Mean 2010–2015 seasonal pattern of natural methane emissions in Tg month^{-1} . The annual total emissions are 14.8
574 Tg a^{-1} (prior, gray), $10.5 \pm 1.9 \text{ Tg a}^{-1}$ (posterior ECCC, blue) and $11.7 \pm 1.2 \text{ Tg a}^{-1}$ (posterior GOSAT, green). The posterior
575 results are within the uncertainty range provided by the WetCHARTS extended ensemble ($3.9\text{--}32.4 \text{ Tg a}^{-1}$ for Canada).

576

577 3.4 Joint-inversions combining ECCC in situ and GOSAT satellite data

578 We combine the ECCC and GOSAT datasets in two policy-themed inversions: (1) optimizing emissions according to the
579 sectors in the national inventory ($n = 5$ state vector elements; corresponding to the categories in Table 2) and (2) optimizing
580 emissions by provinces split into anthropogenic and natural totals ($n = 16$) and show the results in Figure 9. These inversions
581 are under-determined and show the limitations of the ECCC+GOSAT observing system towards constraining very small
582 magnitude emissions in Canada. We conduct the inversions for each year from 2010–2015 individually and present the average
583 from these six samples. Since these two policy inversions use a low number of state vector elements, they are vulnerable to
584 both aggregation error and overfitting of the well-constrained state vector elements and do not necessarily benefit from using
585 a larger data vector from all six years. We discuss the diagnostics and information content for these inversions in detail in
586 Section 1.4 of the Supplement. The error bars are the 1σ standard deviation of the six yearly results and therefore represent
587 both noise in the inversion procedure and year-to-year differences in the state (emissions and/or transport). Here we do not
588 apply a weighting factor to either dataset, the observations are treated equivalently for the cost function in eq. (1). While there
589 are about 5 times more GOSAT observations than ECCC observations for use in our analysis, the in situ observations have



590 larger observational error in S_a (due to model error) are much more sensitive to surface fluxes which offset overweighing the
591 larger amount of GOSAT data. As further diagnostics we show the inversions using GOSAT and ECCC individually (Table
592 S3 and S4) which show general agreement between the datasets. We also use a singular value decomposition eigenanalysis
593 (Heald et al., 2004) to evaluate the independence of the state vector elements and to demonstrate which sectoral categories and
594 provinces can be reliably constrained above the noise in the system (Fig. S4 and S5 in the Supplement).

595

596 Figure 9 (top) shows the sectoral inversion corresponding to categories in the national inventory (Table 2). The prior emissions
597 with 50% error estimates (60% for wetlands) are 2.4 Tg a^{-1} (Energy), 1.0 Tg a^{-1} (Agriculture), 0.9 Tg a^{-1} (Waste), 14.0 Tg a^{-1}
598 (Wetlands) and 0.8 Tg a^{-1} (Other Natural). The posterior emissions are $3.6 \pm 0.9 \text{ Tg a}^{-1}$ (Energy), $1.5 \pm 0.4 \text{ Tg a}^{-1}$ (Agriculture),
599 $0.6 \pm 0.3 \text{ Tg a}^{-1}$ (Waste), $9.4 \pm 1.1 \text{ Tg a}^{-1}$ (Wetlands), and $1.7 \pm 0.9 \text{ Tg a}^{-1}$ (Other Natural). The degrees of freedom for signal
600 and singular value decomposition (Fig. S4) show 3–4 independent pieces of information can be retrieved, which are
601 differentiated in the figure by solid and hatched bars. The singular value decomposition shows strong source signals
602 corresponding to wetlands and energy with signal-to-noise ratios of ~ 37 and ~ 5 , respectively. These are the two largest
603 emissions sources in Canada and show the inverse system can successfully disentangle the major anthropogenic and natural
604 contributors. Emissions from waste have a signal-to-noise ratio of ~ 2 and can be constrained despite the low magnitude of
605 emissions. This is likely due to waste emissions being more concentrated in Central Canada and away from the influence of
606 large energy and agriculture emissions in Western Canada. Emissions from other natural sources are at the noise limit and
607 show a moderate correlation with wetlands, which shows that these two sources are not completely independent. Agriculture
608 emissions are below the noise in the system and highly correlated with energy emissions. This is likely due to the high spatial
609 overlap of energy and agriculture emissions in Western Canada. As a result of these limitations, we present the total of energy
610 and agriculture as $5.1 \pm 1.0 \text{ Tg a}^{-1}$ and the total of wetlands and other natural as $11.1 \pm 1.4 \text{ Tg a}^{-1}$. Our results for total natural
611 and total anthropogenic emissions are consistent with the results from the previous monthly inversion, with the added benefit
612 of identifying which sectors are responsible for the higher anthropogenic emissions at the cost of lower temporal resolution.
613 Waste emissions are 36% lower than the prior and 35% lower than the National GHG Inventory. The total for energy and
614 agriculture is 49% higher than the prior and 59% higher than the total in the inventory. These results show that energy and/or
615 agriculture are the sectors that are responsible for the higher anthropogenic emissions.

616

617 Figure 9 (bottom) shows the provincial inversion corresponding to the six largest emitting provinces (BC British Columbia,
618 AB Alberta, SK, Saskatchewan, MB Manitoba, ON Ontario, QC Quebec) and two aggregated regions (ATL Atlantic Canada,
619 NOR Northern Territories). These regions are further subdivided into total anthropogenic and total natural methane emissions,
620 with below detection limit anthropogenic emissions from Atlantic Canada and Northern Territories. This inversion especially
621 challenges the limitations of the ECCC+GOSAT observation system, as only about 8 of 16 independent pieces of information
622 are retrieved. This means that half of the posterior provincial emissions are below the noise, and we are unable to constrain
623 province-by-province emissions. The singular value decomposition identifies which regions are well constrained (Fig. S5).



624 For the anthropogenic emissions AB and ON are strongly constrained. For the natural emissions AB, ON, SK and MB are well
625 constrained. BC shows correlation between its own anthropogenic and natural emissions and cannot be completely
626 disaggregated. As a result, we group elements together in Western Canada (BC + AB + SA + MB) and Central Canada (ON +
627 QC) for interpretation. The total for Western Canada anthropogenic emissions is $4.6 \pm 0.6 \text{ Tg a}^{-1}$ which is 39% higher than the
628 prior of 3.3 Tg a^{-1} . The total for Central Canada is $0.8 \pm 0.2 \text{ Tg a}^{-1}$ which is 11% lower than the prior of 0.9 Tg a^{-1} .

629

630 Each of our top-down inversion results show higher total anthropogenic emissions than bottom-up estimates. This is consistent
631 regardless of the observation vector incorporating ECCC data, GOSAT data or ECCC+GOSAT data. The subnational scale
632 emissions are limited in their ability to provide full characterization of minor emissions across Canada but can successfully
633 constrain major emissions for source attribution. The sectoral inversion attributes higher anthropogenic emissions to energy
634 and/or agriculture and applies a small decrease to waste emissions. The provincial inversion attributes higher anthropogenic
635 emissions to Western Canada and a small decrease to Central Canada. These results suggest that anthropogenic emissions in
636 Canada are underestimated primarily because of higher emissions from Western Canada energy and/or agriculture. This
637 interpretation is consistent with previous satellite inverse modelling studies over North America that apply positive scaling
638 factors to grid box clusters in Western Canada to match observations (Maasackers et al., 2019; Turner et al., 2015; Wecht et
639 al., 2014). Aircraft studies in Alberta have also shown higher emissions from oil and gas in Alberta than bottom up estimates
640 (Baray et al., 2018; Johnson et al., 2017). Atherton et al. (2017) estimated higher emissions from natural gas in north-eastern
641 British Columbia using mobile surface in situ measurements (Atherton et al., 2017). Zavala-Araiza et al. (2018) showed a
642 significant amount of methane emissions in Alberta from equipment leaks and venting go unreported due to current reporting
643 requirements and in some regions a small number of sites may be responsible for most methane emissions. Our inverse
644 modelling results from 2010–2015 suggest a consistent presence of under-reported or unreported emissions which require a
645 policy adjustment to reporting practices.

646

647

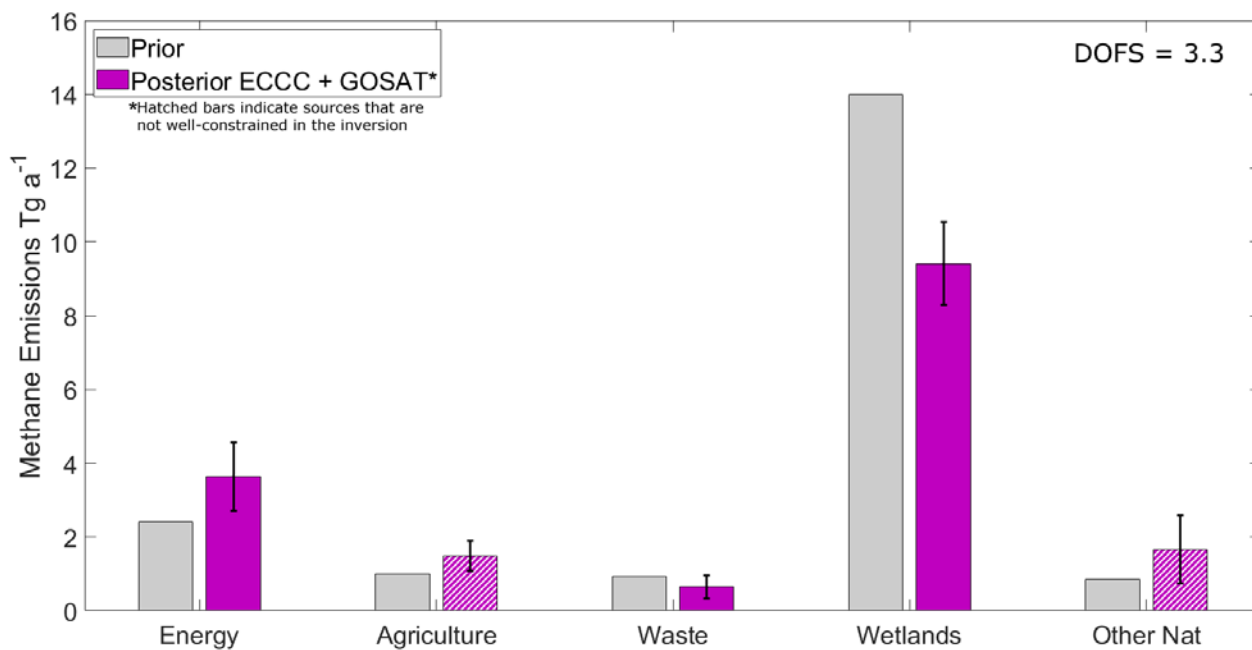
648

649

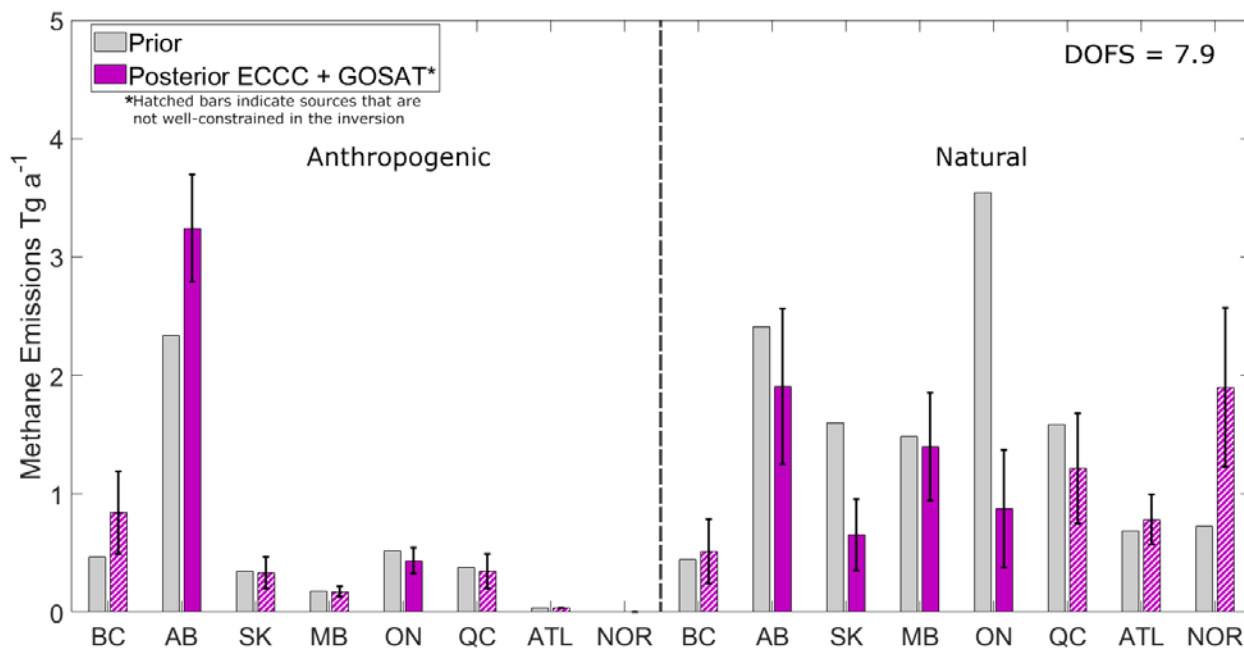
650

651

652



653



654

655

656 **Figure 9:** Joint-inversions combining 2010–2015 ECCC in situ and GOSAT satellite data showing how the combined
 657 observing system remains limited towards resolving all Canadian sources. Inversions are done for each year and we present
 658 the six-year average with error bars showing the 1 σ standard deviation of the yearly results. Hatched bars indicate sources that
 659 are not well-constrained, these are defined as state vector elements with averaging kernel sensitivities less than 0.8 which are



660 affected by aliasing with other sources (See Supplemental Fig. S4 and S5). The top panel shows the sectoral inversion
661 according to the categories in the National GHG inventory (Energy, Agriculture, Waste) and two natural categories (Wetlands
662 and Other Natural). As an example, the diagnostics in Figure S4 shows Agriculture emissions are beneath the noise and cannot
663 be distinguished from Energy. The bottom panel shows the subnational regional inversion according to provinces (BC British
664 Columbia, AB Alberta, SK, Saskatchewan, MB Manitoba, ON Ontario, QC Quebec) and aggregated regions (ATL Atlantic
665 Canada, NOR Northern Territories) further subdivided according to total anthropogenic and total natural emissions. The
666 diagnostics in Fig. S5 show more than half of the regions are at or below the noise. For anthropogenic emissions, the best
667 constraints are on provinces AB and ON. For natural emissions, the best constraints are on AB, SK, MB and ON.

668 3.5 Comparison to Independent Aircraft and In situ Data

669 We test the robustness of the optimized emissions from each of the three inversions shown (monthly natural, sectoral, and
670 provincial) by comparing to independent measurements not used in the inversions. Prior and posterior simulated methane
671 concentrations are compared to measurements from NOAA ESRL aircraft profiles at East Trout Lake, Saskatchewan (Mund
672 et al., 2017) and ECCC surface measurements in sites Chapais and Chibougamau in Quebec, Canada. The surface data was
673 averaged to daily afternoon means (12:00 to 16:00 local time) in the same manner as the surface measurements used in the
674 inversion. Aircraft data from the NOAA ESRL profiles coincide spatially with the surface measurements at ETL through a
675 joint analysis program with Environment and Climate Change Canada and have occurred on a regular basis approximately
676 once a month from 2005 until present time. Aircraft measurements reach ~7000 m above the surface with samples at multiple
677 altitudes accomplished using a programmable multi-flask system that is further discussed in Mund et al. (2017), however we
678 limit the comparison to the lowest 1 km above ground since higher altitude measurements are mostly background. The aircraft
679 data is not averaged however the flights occur around the same time in the early afternoon.

680

681 Figure 10 shows the comparison using reduced-major axis (RMA) regressions with the coefficient of determination (R^2), the
682 slope and the mean-bias shown as metrics to evaluate the agreement. Surface data in CHA, Quebec shows better posterior
683 agreement with observations according to all metrics for each of the three inversions. The R^2 of the prior is 0.36 and improves
684 to a range of 0.44–0.52 for the posterior results, the slope is 1.17 in the prior and improves to a range of 0.91–1.13 and the
685 mean bias is –16.4 ppb in the prior and improves to –11.4 and –4.9 ppb. Since this site in Quebec is particularly sensitive to
686 the Hudson Bay Lowlands, the agreement in all metrics suggests our posterior emissions can better represent wetlands
687 emissions in this region. This includes the reduced peak seasonality of natural emissions in the monthly inversion, the reduction
688 of wetlands emissions in the sectoral inversion or the reduction of natural emissions primarily in Central Canada in the
689 provincial inversion. Aircraft data in Saskatchewan shows improvement in the R^2 and mean bias metrics but slightly degrades
690 the slope in one case. The R^2 of the prior is 0.14 and improves to a range of 0.20–0.33, the mean bias of the prior is –6.8ppb
691 and improves to –0.4 and –1.4 ppb. The slope of the prior is 1.15 which slightly degrades to 0.83 in the monthly inversion and
692 improves to a range of 0.86–0.91 in the provincial and sectoral inversions. The high resolution aircraft measurements are more

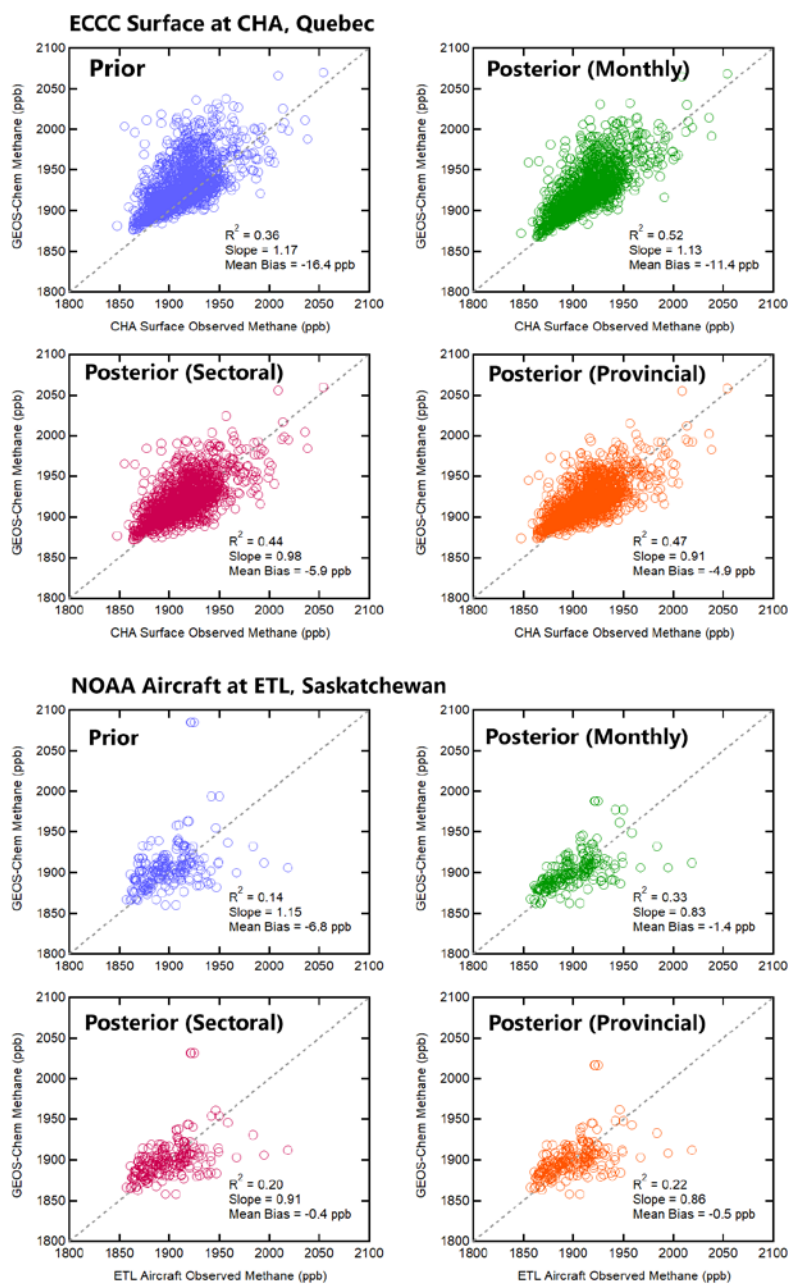


693 susceptible to representation error at this $2^{\circ}\times 2.5^{\circ}$ grid resolution. Furthermore, the time-series comparison to surface data at
694 East Trout Lake (Fig. 6) shows overall lower sensitivity to summertime wetlands emissions than Fraserdale and Egbert, and
695 lower sensitivity to anthropogenic emissions from Alberta than Lac La Biche. Hence the modelled methane concentrations at
696 the aircraft measurement points are adjusted less by the change in posterior emissions. However, improvement in the R^2 and
697 mean bias metrics show there is still a better representation of the variance in the data which suggests the posterior emissions
698 reduce bias due to peak emission episodes.

699

700

701



702

703 **Figure 10:** Evaluation of inversion results with reduced-major axis (RMA) regressions using independent data. The top four
 704 panels show the comparison to ECCC surface observations at Chapais and Chibougamau in Quebec, Canada and the bottom
 705 four panels show the comparison to NOAA aircraft profiles at East Trout Lake, Saskatchewan. The agreement of observations
 706 with prior simulated methane concentrations (blue) are compared to posterior concentrations using optimized emissions from
 707 the monthly inversion (green), the sectoral inversion (magenta), and the provincial inversion (orange). The coefficient of
 708 determination (R^2), slope and mean bias are shown as metrics of agreement.



709 4 Conclusions

710 We conduct a Bayesian inverse analysis to optimize anthropogenic and natural methane emissions in Canada using 2010–2015
711 ECCC in situ and GOSAT satellite observations in GEOS-Chem. Methane concentrations are simulated on a $2^\circ \times 2.5^\circ$ grid
712 using recently updated prior emissions inventories for energy and wetlands emissions in Canada. Modelled background
713 conditions for the Canadian domain are shown to be unbiased in the comparison to surface in situ data at the western most site
714 in Canada, Estevan point, with agreement within 6 ppb. A forward model analysis shows much larger biases between -100
715 ppb and $+1050$ ppb at surface sites throughout Canada demonstrating the presence of misrepresented local emissions. We
716 show large positive biases (overestimation of emissions) in the summertime are observed at sites sensitive to wetlands
717 emissions, these biases are reduced by using lower magnitude wetlands emissions scenarios with lower CH_4 :C temperature
718 sensitivities or lower inundation extent. We also show the opposite case of negative biases (underestimation of emissions)
719 observed year-round at sites in Western Canada. The forward model analysis is consistent with the results of the inverse
720 analysis that reduce emissions from natural sources and increase emissions from anthropogenic sources to minimize the
721 mismatch between modelled and observed methane.

722

723 We show three approaches for using ECCC and GOSAT data towards inverse modelling of Canadian methane emissions.
724 These approaches differ according to the temporal and spatial resolution of the solution. We show: (1) a high time-resolution
725 inversion that solves for natural emissions each month from 2010–2015 and anthropogenic emissions as yearly totals, (2) a
726 sectoral inversion that solves for emissions according to categories in the national inventory, (3) a provincial inversion that
727 solves for total anthropogenic and natural emissions at the subnational level. The monthly inversion provides information on
728 the seasonality of natural emissions (which are $\sim 95\%$ wetlands) but does not provide more depth into anthropogenic emissions
729 beyond yearly scaling. The sectoral inversion provides more information on the categories of anthropogenic emissions that are
730 misrepresented in the prior but without spatial detail. The provincial inversion provides the highest level of spatial
731 discretization but is largely underdetermined due to the limitations of the observing system towards characterizing very low
732 magnitude emissions from smaller contributing provinces.

733

734 Inversion results (1) show mean 2010–2015 posterior emissions for total anthropogenic sources in Canada are $6.0 \pm 0.4 \text{ Tg a}^{-1}$
735 ¹ using ECCC data and $6.5 \pm 0.7 \text{ Tg a}^{-1}$ using GOSAT data. Annual mean natural emissions are $10.5 \pm 1.9 \text{ Tg a}^{-1}$ using ECCC
736 data and $11.7 \pm 1.2 \text{ Tg a}^{-1}$ using GOSAT data. Both inverse modelling estimates are higher than the prior for anthropogenic
737 emissions 4.4 Tg a^{-1} and lower than the prior for natural emissions 14.8 Tg a^{-1} . Inversion results using both datasets show a
738 change in the seasonal profile of natural methane emissions where emissions are slower to begin in the spring and show a less
739 intense peak in the summer. The agreement between two datasets assembled with different measurement methodologies that
740 sample different parts of the atmosphere is a robust result that lends weight to our conclusions. Our results corroborate recent
741 studies showing a less-intense and less-narrow summertime peak in North American Boreal wetlands emissions with a higher



742 relative contribution from the cold season (Miller et al., 2016; Zona et al., 2016; Warwick et al., 2016; Thonat et al., 2017;
743 Treat et al., 2018; Peltola et al., 2019). These top-down studies using atmospheric observations show biosphere process models
744 can better account for a more complex response to peak surface soil temperatures.

745

746 We also conduct combined ECCC+GOSAT inversions that aim to resolve finer resolution emissions corresponding to (2) the
747 sectors of the national inventory and corresponding to (3) provincial boundaries. These policy-themed inversions challenge
748 the capabilities of the ECCC+GOSAT observation system and show the system is not capable of resolving many minor
749 emissions in Canada. The degrees of freedom for signal for these inversions are 3–4 out of 5 state vector elements for the
750 sectoral inversion and 8 out of 16 for the provincial inversion. The limitation of this inverse approach towards constraining
751 sectoral or regional scale emissions in Canada is due to the low magnitude of these emissions, their overlapping nature in
752 concentrated regions, and the sparsity of data available to distinguish them apart. Grouping correlated sectors together, we
753 determine $5.1 \pm 1.0 \text{ Tg a}^{-1}$ for energy and agriculture which is 59% higher than the inventory, $0.6 \pm 0.3 \text{ Tg a}^{-1}$ for waste which
754 is 35% lower than the inventory. For provincial emissions, we show Western Canada is $4.6 \pm 0.6 \text{ Tg a}^{-1}$ which is 39% higher
755 than the prior and Central Canada is 0.8 ± 0.2 which is 11% lower. Both regions show lower natural emissions. These results
756 show that the higher anthropogenic emissions in the posterior results can be attributed to energy and/or agriculture primarily
757 in Western Canada where most of Canadian anthropogenic emissions are concentrated. Our results are consistent with other
758 top-down studies that show higher than reported anthropogenic emissions in Western Canada (Wecht et al., 2014; Turner et
759 al., 2015; Atherton et al., 2017; Johnson et al., 2017; Baray et al., 2018; Maasackers et al., 2019). This may be due to oil and
760 gas emissions that are under-reported or unreported due to current reporting requirements (Zavala-Araiza et al., 2018). These
761 top-down studies show a need for policy readjustment in reporting practices for Canadian anthropogenic methane emissions.

762

763 This study shows the value of using complementary surface and satellite datasets in an inverse analysis. We emphasize the
764 value of comparative analysis using the datasets independently versus as joint inversions, as minor emissions are too low in
765 magnitude for the observational precision to distinguish finer scale discretization above the noise. The comparative analysis
766 has the added benefit of evaluating the datasets against each other and the assumptions that are specific to using either surface
767 or satellite data. The capabilities for combining and intercomparing datasets is expected to improve, with the launch of
768 Copernicus Sentinel-5p satellite (TROPOMI) in 2017 and continued expansions on in situ observation networks. The ability
769 for next generation observations to constrain subnational level emissions in Canada will depend on instrument and model
770 precision, as well as the emissions magnitudes and spatiotemporal overlap of the targets. These technical capabilities should
771 be weighed alongside policy needs for improved methane monitoring.

772



773 **Competing Interests**

774 The authors declare that they have no conflict of interest.

775 **Data Availability**

776 GEOS-Chem is from <http://acmg.seas.harvard.edu/geos/> which includes links to all gridded prior emissions and
777 meteorological fields used in this analysis. GOSAT satellite data is from the University of Leicester v7 proxy retrieval is
778 available through the Copernicus Climate Change Service <https://climate.copernicus.eu/>. ECCC in situ data is available
779 through the World Data Centre for Greenhouse Gases (WDCGG) <https://gaw.kishou.go.jp/>. NOAA/ESRL aircraft data is
780 from the Global Monitoring Laboratory <https://www.esrl.noaa.gov/gmd/ccgg/aircraft/>.

781 **Author Contributions**

782 SB, DJJ and RM designed the study. SB conducted the simulations and analysis with contributions from JDM, JXS, MPS,
783 and DBAJ. AAB provided WetCHARTS emissions and supporting data. SB and RM wrote the paper with contributions
784 from all authors. RM was responsible for funding acquisition at York U while DJJ acquired funding at Harvard U.

785 **Acknowledgements**

786 Work at Harvard was supported by the NASA Carbon Monitoring System. We thank the Japanese Aerospace Exploration
787 Agency (JAXA) responsible for the GOSAT instrument, and the University of Leicester for the retrieval algorithm used in
788 this analysis. Doug Worthy and the Climate Research Division at Environment and Climate Change Canada are responsible
789 for the in situ surface measurements and the NOAA/ESRL program is responsible for the aircraft methane measurements.
790



791 **References**

- 792 Atherton, E., Risk, D., Fougère, C., Lavoie, M., Marshall, A., Werring, J., Williams, J. P. and Minions, C.: Mobile
793 measurement of methane emissions from natural gas developments in northeastern British Columbia, Canada, *Atmos. Chem.*
794 *Phys.*, 17(20), 12405–12420, doi:10.5194/acp-17-12405-2017, 2017.
- 795 Baray, S., Darlington, A., Gordon, M., Hayden, K. L., Leithead, A., Li, S.-M., Liu, P. S. K., Mittermeier, R. L., Moussa, S.
796 G., O'Brien, J., Staebler, R., Wolde, M., Worthy, D. and McLaren, R.: Quantification of methane sources in the Athabasca Oil
797 Sands Region of Alberta by aircraft mass balance, *Atmos. Chem. Phys.*, 18(10), 7361–7378, doi:10.5194/acp-18-7361-2018,
798 2018.
- 799 Bloom, A. A., Bowman, K. W., Lee, M., Turner, A. J., Schroeder, R., Worden, J. R., Weidner, R., McDonald, K. C. and Jacob,
800 D. J.: A global wetland methane emissions and uncertainty dataset for atmospheric chemical transport models (WetCHARTs
801 version 1.0), *Geosci. Model Dev.*, 10(6), 2141–2156, doi:10.5194/gmd-10-2141-2017, 2017.
- 802 Bubier, J. L., Moore, T. R. and Roulet, N. T.: Methane Emissions from Wetlands in the Midboreal Region of Northern Ontario,
803 Canada, *Ecology*, 74(8), 2240–2254, doi:10.2307/1939577, 1993.
- 804 Buchwitz, M., Reuter, M., Schneising, O., Boesch, H., Guerlet, S., Dils, B., Aben, I., Armante, R., Bergamaschi, P.,
805 Blumenstock, T., Bovensmann, H., Brunner, D., Buchmann, B., Burrows, J. P., Butz, A., Chédin, A., Chevallier, F., Crevoisier,
806 C. D., Deutscher, N. M., Frankenberg, C., Hase, F., Hasekamp, O. P., Heymann, J., Kaminski, T., Laeng, A., Lichtenberg, G.,
807 De Mazière, M., Noël, S., Notholt, J., Orphal, J., Popp, C., Parker, R., Scholze, M., Sussmann, R., Stiller, G. P., Warneke, T.,
808 Zehner, C., Bril, A., Crisp, D., Griffith, D. W. T., Kuze, A., O'Dell, C., Oshchepkov, S., Sherlock, V., Suto, H., Wennberg,
809 P., Wunch, D., Yokota, T. and Yoshida, Y.: The Greenhouse Gas Climate Change Initiative (GHG-CCI): Comparison and
810 quality assessment of near-surface-sensitive satellite-derived CO₂ and CH₄ global data sets, *Remote Sensing of Environment*,
811 162, 344–362, doi:10.1016/j.rse.2013.04.024, 2015.
- 812 Chanton, J. and Liptay, K.: Seasonal variation in methane oxidation in a landfill cover soil as determined by an in situ stable
813 isotope technique, *Global Biogeochem. Cycles*, 14(1), 51–60, doi:10.1029/1999GB900087, 2000.
- 814 Dlugokencky, E. J., Bruhwiler, L., White, J. W. C., Emmons, L. K., Novelli, P. C., Montzka, S. A., Masarie, K. A., Lang, P.
815 M., Croftwell, A. M., Miller, J. B. and Gatti, L. V.: Observational constraints on recent increases in the atmospheric CH₄
816 burden, *Geophys. Res. Lett.*, 36(18), L18803, doi:10.1029/2009GL039780, 2009.
- 817 Environment and Climate Change Canada: National Inventory Report 1990–2015: Greenhouse Gas Sources and Sinks in
818 Canada, Canada's Submission to the United Nations Framework Convention on Climate Change, Part 3. Available at:
819 http://publications.gc.ca/collections/collection_2018/eccc/En81-4-2015-3-eng.pdf, 2017.



- 820 ESA CCI GHG project team: ESA Greenhouse Gases Climate Change Initiative (GHG_cci): Column-averaged CH₄ from
821 GOSAT generated with the OCPR (UoL-PR) Proxy algorithm (CH₄_GOS_OCPR), v7.0. Centre for Environmental Data
822 Analysis, Available at: <https://catalogue.ceda.ac.uk/uuid/f9154243fd8744bdaf2a59c39033e659>, 2018.
- 823 Fung, I., John, J., Lerner, J., Matthews, E., Prather, M., Steele, L. P. and Fraser, P. J.: Three-dimensional model synthesis of
824 the global methane cycle, *J. Geophys. Res.*, 96(D7), 13033, doi:10.1029/91JD01247, 1991.
- 825 Hartmann, D. L., Tank, A. M. K., Rusticucci, M., Alexander, L. V., Brönnimann, S., Charabi, Y. A. R., Dentener, F. J.,
826 Dlugokencky, E. J., Easterling, D. R., Kaplan, A., Soden, B. J., Thorne, P. W., Wild, M., and Zhai, P. M.: Observations:
827 atmosphere and surface, in: *Climate Change 2013 the Physical Science Basis: Working Group I Contribution to the Fifth*
828 *Assessment Report of the Intergovernmental Panel on Climate Change*, Cambridge University Press, 2013.
- 829 Hausmann, P., Sussmann, R. and Smale, D.: Contribution of oil and natural gas production to renewed increase in atmospheric
830 methane (2007–2014): top–down estimate from ethane and methane column observations, *Atmos. Chem. Phys.*, 16(5), 3227–
831 3244, doi:10.5194/acp-16-3227-2016, 2016.
- 832 Heald, C. L., Jacob, D. J., Jones, D. B. A., Palmer, P. I., Logan, J. A., Streets, D. G., Sachse, G. W., Gille, J. C., Hoffman, R.
833 N. and Nehr Korn, T.: Comparative inverse analysis of satellite (MOPITT) and aircraft (TRACE-P) observations to estimate
834 Asian sources of carbon monoxide: COMPARATIVE INVERSE ANALYSIS, *J. Geophys. Res.*, 109(D23),
835 doi:10.1029/2004JD005185, 2004.
- 836 Hu, H., Landgraf, J., Detmers, R., Borsdorff, T., Aan de Brugh, J., Aben, I., Butz, A. and Hasekamp, O.: Toward Global
837 Mapping of Methane With TROPOMI: First Results and Intersatellite Comparison to GOSAT, *Geophys. Res. Lett.*, 45(8),
838 3682–3689, doi:10.1002/2018GL077259, 2018.
- 839 Ishizawa, M., Chan, D., Worthy, D., Chan, E., Vogel, F. and Maksyutov, S.: Analysis of atmospheric CH₄ in Canadian Arctic
840 and estimation of the regional CH₄ fluxes, *Atmos. Chem. Phys.*, 19(7), 4637–4658, doi:10.5194/acp-19-4637-2019, 2019.
- 841 Jacob, D. J., Turner, A. J., Maasackers, J. D., Sheng, J., Sun, K., Liu, X., Chance, K., Aben, I., McKeever, J. and Frankenberg,
842 C.: Satellite observations of atmospheric methane and their value for quantifying methane emissions, *Atmos. Chem. Phys.*,
843 16(22), 14371–14396, doi:10.5194/acp-16-14371-2016, 2016.
- 844 Johnson, M. R., Tyner, D. R., Conley, S., Schwietzke, S. and Zavala-Araiza, D.: Comparisons of Airborne Measurements and
845 Inventory Estimates of Methane Emissions in the Alberta Upstream Oil and Gas Sector, *Environ. Sci. Technol.*, 51(21), 13008–
846 13017, doi:10.1021/acs.est.7b03525, 2017.
- 847 Kirschke, S., Bousquet, P., Ciais, P., Saunois, M., Canadell, J. G., Dlugokencky, E. J., Bergamaschi, P., Bergmann, D., Blake,
848 D. R., Bruhwiler, L., Cameron-Smith, P., Castaldi, S., Chevallier, F., Feng, L., Fraser, A., Heimann, M., Hodson, E. L.,
849 Houweling, S., Josse, B., Fraser, P. J., Krummel, P. B., Lamarque, J.-F., Langenfelds, R. L., Le Quééré, C., Naik, V., O’Doherty,



- 850 S., Palmer, P. I., Pison, I., Plummer, D., Poulter, B., Prinn, R. G., Rigby, M., Ringeval, B., Santini, M., Schmidt, M., Shindell,
851 D. T., Simpson, I. J., Spahni, R., Steele, L. P., Strode, S. A., Sudo, K., Szopa, S., van der Werf, G. R., Voulgarakis, A., van
852 Weele, M., Weiss, R. F., Williams, J. E. and Zeng, G.: Three decades of global methane sources and sinks, *Nature Geosci.*,
853 6(10), 813–823, doi:10.1038/ngeo1955, 2013.
- 854 Lu, X., Jacob, D. J., Zhang, Y., Maasackers, J. D., Sulprizio, M. P., Shen, L., Qu, Z., Scarpelli, T. R., Nesser, H., Yantosca,
855 R. M., Sheng, J., Andrews, A., Parker, R. J., Boech, H., Bloom, A. A., and Ma, S.: Global methane budget and trend, 2010–
856 2017: complementarity of inverse analyses using in situ (GLOBALVIEWplus CH₄ ObsPack) and satellite (GOSAT)
857 observations, *Atmos. Chem. Phys. Discuss.*, <https://doi.org/10.5194/acp-2020-775>, in review, 2020.
- 858 Maasackers, J. D., Jacob, D. J., Sulprizio, M. P., Turner, A. J., Weitz, M., Wirth, T., Hight, C., DeFigueiredo, M., Desai, M.,
859 Schmeltz, R., Hockstad, L., Bloom, A. A., Bowman, K. W., Jeong, S. and Fischer, M. L.: Gridded National Inventory of U.S.
860 Methane Emissions, *Environ. Sci. Technol.*, 50(23), 13123–13133, doi:10.1021/acs.est.6b02878, 2016.
- 861 Maasackers, J. D., Jacob, D. J., Sulprizio, M. P., Scarpelli, T. R., Nesser, H., Sheng, J.-X., Zhang, Y., Hersher, M., Bloom, A.
862 A., Bowman, K. W., Worden, J. R., Janssens-Maenhout, G. and Parker, R. J.: Global distribution of methane emissions,
863 emission trends, and OH concentrations and trends inferred from an inversion of GOSAT satellite data for 2010–2015, *Atmos.*
864 *Chem. Phys.*, 19(11), 7859–7881, doi:10.5194/acp-19-7859-2019, 2019.
- 865 Maasackers, J. D., Jacob, D. J., Sulprizio, M. P., Scarpelli, T. R., Nesser, H., Sheng, J., Zhang, Y., Lu, X., Bloom, A. A.,
866 Bowman, K. W., Worden, J. R., and Parker, R. J.: 2010–2015 North American methane emissions, sectoral contributions, and
867 trends: a high-resolution inversion of GOSAT satellite observations of atmospheric methane, *Atmos. Chem. Phys. Discuss.*,
868 <https://doi.org/10.5194/acp-2020-915>, in review, 2020.
- 869 Miller, S. M., Worthy, D. E. J., Michalak, A. M., Wofsy, S. C., Kort, E. A., Havice, T. C., Andrews, A. E., Dlugokencky, E.
870 J., Kaplan, J. O., Levi, P. J., Tian, H. and Zhang, B.: Observational constraints on the distribution, seasonality, and
871 environmental predictors of North American boreal methane emissions, *Global Biogeochem. Cycles*, 28(2), 146–160,
872 doi:10.1002/2013GB004580, 2014.
- 873 Miller, S. M., Commane, R., Melton, J. R., Andrews, A. E., Benmergui, J., Dlugokencky, E. J., Janssens-Maenhout, G.,
874 Michalak, A. M., Sweeney, C. and Worthy, D. E. J.: Evaluation of wetland methane emissions across North America using
875 atmospheric data and inverse modeling, *Biogeosciences*, 13(4), 1329–1339, doi:10.5194/bg-13-1329-2016, 2016.
- 876 Moore, T. R., Heyes, A. and Roulet, N. T.: Methane emissions from wetlands, southern Hudson Bay lowland, *J. Geophys.*
877 *Res.*, 99(D1), 1455, doi:10.1029/93JD02457, 1994.
- 878 Mund, J., Thoning, K., Tans, P., Sweeny, C., Higgs, J., Wolter, S., Crotwell, A., Neff, D., Dlugokencky, E., Lang, P., Novelli,
879 P., Moglia, E. and Crotwell, M.: Earth System Research Laboratory Carbon Cycle and Greenhouse Gases Group Flask-Air



- 880 Sample Measurements of CO₂, CH₄, CO, N₂O, H₂, and SF₆ from the Aircraft Program, 1992-Present, ,
881 doi:10.7289/V5N58JMF, 2017.
- 882 Myhre, G.: Anthropogenic and Natural Radiative Forcing, in *Climate Change 2013: The Physical Science Basis. Contribution*
883 *of Working Group I to the Fifth Assessment Report of the Intergovernmental Panel on Climate Change.*, 2013.
- 884 Nisbet, E. G., Dlugokencky, E. J., Manning, M. R., Lowry, D., Fisher, R. E., France, J. L., Michel, S. E., Miller, J. B., White,
885 J. W. C., Vaughn, B., Bousquet, P., Pyle, J. A., Warwick, N. J., Cain, M., Brownlow, R., Zazzeri, G., Lanoisellé, M., Manning,
886 A. C., Gloor, E., Worthy, D. E. J., Brunke, E.-G., Labuschagne, C., Wolff, E. W. and Ganesan, A. L.: Rising atmospheric
887 methane: 2007-2014 growth and isotopic shift: RISING METHANE 2007-2014, *Global Biogeochem. Cycles*, 30(9), 1356–
888 1370, doi:10.1002/2016GB005406, 2016.
- 889 Nisbet, E. G., Fisher, R. E., Lowry, D., France, J. L., Allen, G., Bakkaloglu, S., Broderick, T. J., Cain, M., Coleman, M.,
890 Fernandez, J., Forster, G., Griffiths, P. T., Iverach, C. P., Kelly, B. F. J., Manning, M. R., Nisbet-Jones, P. B. R., Pyle, J. A.,
891 Townsend-Small, A., al-Shalaan, A., Warwick, N. and Zazzeri, G.: Methane Mitigation: Methods to Reduce Emissions, on the
892 Path to the Paris Agreement, *Rev. Geophys.*, 58(1), doi:10.1029/2019RG000675, 2020.
- 893 Patra, P. K., Houweling, S., Krol, M., Bousquet, P., Belikov, D., Bergmann, D., Bian, H., Cameron-Smith, P., Chipperfield,
894 M. P., Corbin, K., Fortems-Cheiney, A., Fraser, A., Gloor, E., Hess, P., Ito, A., Kawa, S. R., Law, R. M., Loh, Z., Maksyutov,
895 S., Meng, L., Palmer, P. I., Prinn, R. G., Rigby, M., Saito, R. and Wilson, C.: TransCom model simulations of CH₄ and related
896 species: linking transport, surface flux and chemical loss with CH₄ variability in the troposphere and lower stratosphere,
897 *Atmos. Chem. Phys.*, 11(24), 12813–12837, doi:10.5194/acp-11-12813-2011, 2011.
- 898 Peltola, O., Vesala, T., Gao, Y., Rätty, O., Alekseychik, P., Aurela, M., Chojnicki, B., Desai, A. R., Dolman, A. J., Euskirchen,
899 E. S., Friborg, T., Göckede, M., Helbig, M., Humphreys, E., Jackson, R. B., Jocher, G., Joos, F., Klatt, J., Knox, S. H.,
900 Kowalska, N., Kutzbach, L., Lienert, S., Lohila, A., Mammarella, I., Nadeau, D. F., Nilsson, M. B., Oechel, W. C., Peichl, M.,
901 Pypker, T., Quinton, W., Rinne, J., Sachs, T., Samson, M., Schmid, H. P., Sonntag, O., Wille, C., Zona, D. and Aalto, T.:
902 Monthly gridded data product of northern wetland methane emissions based on upscaling eddy covariance observations, *Earth*
903 *Syst. Sci. Data*, 11(3), 1263–1289, doi:10.5194/essd-11-1263-2019, 2019.
- 904 Pickett-Heaps, C. A., Jacob, D. J., Wecht, K. J., Kort, E. A., Wofsy, S. C., Diskin, G. S., Worthy, D. E. J., Kaplan, J. O., Bey,
905 I. and Drevet, J.: Magnitude and seasonality of wetland methane emissions from the Hudson Bay Lowlands (Canada), *Atmos.*
906 *Chem. Phys.*, 11(8), 3773–3779, doi:10.5194/acp-11-3773-2011, 2011.
- 907 Poulter, B., Bousquet, P., Canadell, J. G., Ciais, P., Pregon, A., Saunio, M., Arora, V. K., Beerling, D. J., Brovkin, V., Jones,
908 C. D., Joos, F., Gedney, N., Ito, A., Kleinen, T., Koven, C. D., McDonald, K., Melton, J. R., Peng, C., Peng, S., Prigent, C.,
909 Schroeder, R., Riley, W. J., Saito, M., Spahni, R., Tian, H., Taylor, L., Viovy, N., Wilton, D., Wiltshire, A., Xu, X., Zhang,



- 910 B., Zhang, Z. and Zhu, Q.: Global wetland contribution to 2000–2012 atmospheric methane growth rate dynamics, Environ.
911 Res. Lett., 12(9), 094013, doi:10.1088/1748-9326/aa8391, 2017.
- 912 Prather, M. J., Holmes, C. D. and Hsu, J.: Reactive greenhouse gas scenarios: Systematic exploration of uncertainties and the
913 role of atmospheric chemistry: ATMOSPHERIC CHEMISTRY AND GREENHOUSE GASES, Geophys. Res. Lett., 39(9),
914 n/a-n/a, doi:10.1029/2012GL051440, 2012.
- 915 Rigby, M., Montzka, S. A., Prinn, R. G., White, J. W. C., Young, D., O'Doherty, S., Lunt, M. F., Ganesan, A. L., Manning,
916 A. J., Simmonds, P. G., Salameh, P. K., Harth, C. M., Mühle, J., Weiss, R. F., Fraser, P. J., Steele, L. P., Krummel, P. B.,
917 McCulloch, A. and Park, S.: Role of atmospheric oxidation in recent methane growth, Proc Natl Acad Sci USA, 114(21),
918 5373–5377, doi:10.1073/pnas.1616426114, 2017.
- 919 Rodgers, C. D.: Inverse Methods for Atmospheric Sounding: Theory and Practice, WORLD SCIENTIFIC., 2000.
- 920 Rogelj, J., Popp, A., Calvin, K. V., Luderer, G., Emmerling, J., Gernaat, D., Fujimori, S., Strefler, J., Hasegawa, T., Marangoni,
921 G., Krey, V., Kriegler, E., Riahi, K., van Vuuren, D. P., Doelman, J., Drouet, L., Edmonds, J., Fricko, O., Harmsen, M., Havlík,
922 P., Humpenöder, F., Stehfest, E. and Tavoni, M.: Scenarios towards limiting global mean temperature increase below 1.5 °C,
923 Nature Clim Change, 8(4), 325–332, doi:10.1038/s41558-018-0091-3, 2018.
- 924 Sheng, J.-X., Jacob, D. J., Maasackers, J. D., Sulprizio, M. P., Zavala-Araiza, D. and Hamburg, S. P.: A high-resolution (0.1°
925 × 0.1°) inventory of methane emissions from Canadian and Mexican oil and gas systems, Atmospheric Environment, 158,
926 211–215, doi:10.1016/j.atmosenv.2017.02.036, 2017.
- 927 Sheng, J.-X., Jacob, D. J., Turner, A. J., Maasackers, J. D., Benmergui, J., Bloom, A. A., Arndt, C., Gautam, R., Zavala-Araiza,
928 D., Boesch, H. and Parker, R. J.: 2010–2016 methane trends over Canada, the United States, and Mexico observed by the
929 GOSAT satellite: contributions from different source sectors, Atmos. Chem. Phys., 18(16), 12257–12267, doi:10.5194/acp-
930 18-12257-2018, 2018a.
- 931 Sheng, J.-X., Jacob, D. J., Turner, A. J., Maasackers, J. D., Sulprizio, M. P., Bloom, A. A., Andrews, A. E. and Wunch, D.:
932 High-resolution inversion of methane emissions in the Southeast US using SEAC 4 RS aircraft observations of atmospheric
933 methane: anthropogenic and wetland sources, Atmos. Chem. Phys., 18(9), 6483–6491, doi:10.5194/acp-18-6483-2018, 2018b.
- 934 Stanevich, I., Jones, D. B. A., Strong, K., Keller, M., Henze, D. K., Parker, R. J., Boesch, H., Wunch, D., Notholt, J., Petri, C.,
935 Warneke, T., Sussmann, R., Schneider, M., Hase, F., Kivi, R., Deutscher, N. M., Velazco, V. A., Walker, K. A. and Deng, F.:
936 Characterizing model errors in chemical transport modelling of methane: Using GOSAT XCH4 data with weak constraint
937 four-dimensional variational data assimilation, preprint, Gases/Atmospheric Modelling/Troposphere/Chemistry (chemical
938 composition and reactions), 2019.



- 939 Sweeney, C., Dlugokencky, E., Miller, C. E., Wofsy, S., Karion, A., Dinardo, S., Chang, R. Y.-W., Miller, J. B., Bruhwiler,
940 L., Crotwell, A. M., Newberger, T., McKain, K., Stone, R. S., Wolter, S. E., Lang, P. E. and Tans, P.: No significant increase
941 in long-term CH₄ emissions on North Slope of Alaska despite significant increase in air temperature: LONG-TERM CH₄
942 EMISSIONS ON NORTH SLOPE, *Geophys. Res. Lett.*, 43(12), 6604–6611, doi:10.1002/2016GL069292, 2016.
- 943 Thonat, T., Saunois, M., Bousquet, P., Pison, I., Tan, Z., Zhuang, Q., Crill, P. M., Thornton, B. F., Bastviken, D., Dlugokencky,
944 E. J., Zimov, N., Laurila, T., Hatakka, J., Hermansen, O. and Worthy, D. E. J.: Detectability of Arctic methane sources at six
945 sites performing continuous atmospheric measurements, *Atmos. Chem. Phys.*, 17(13), 8371–8394, doi:10.5194/acp-17-8371-
946 2017, 2017.
- 947 Treat, C. C., Bloom, A. A. and Marushchak, M. E.: Nongrowing season methane emissions—a significant component of annual
948 emissions across northern ecosystems, *Glob Change Biol*, 24(8), 3331–3343, doi:10.1111/gcb.14137, 2018.
- 949 Tunnicliffe, R. L., Ganesan, A. L., Parker, R. J., Boesch, H., Gedney, N., Poulter, B., Zhang, Z., Lavrič, J. V., Walter, D.,
950 Rigby, M., Henne, S., Young, D., and O'Doherty, S.: Quantifying sources of Brazil's CH₄ emissions between 2010 and 2018
951 from satellite data, *Atmos. Chem. Phys.*, 20, 13041–13067, <https://doi.org/10.5194/acp-20-13041-2020>, 2020. Turner, A. J.
952 and Jacob, D. J.: Balancing aggregation and smoothing errors in inverse models, *Atmos. Chem. Phys.*, 15(12), 7039–7048,
953 doi:10.5194/acp-15-7039-2015, 2015.
- 954 Turner, A. J., Jacob, D. J., Wecht, K. J., Maasackers, J. D., Lundgren, E., Andrews, A. E., Biraud, S. C., Boesch, H., Bowman,
955 K. W., Deutscher, N. M., Dubey, M. K., Griffith, D. W. T., Hase, F., Kuze, A., Notholt, J., Ohyama, H., Parker, R., Payne, V.
956 H., Sussmann, R., Sweeney, C., Velazco, V. A., Warneke, T., Wennberg, P. O. and Wunch, D.: Estimating global and North
957 American methane emissions with high spatial resolution using GOSAT satellite data, *Atmos. Chem. Phys.*, 15(12), 7049–
958 7069, doi:10.5194/acp-15-7049-2015, 2015.
- 959 Turner, A. J., Frankenberg, C., Wennberg, P. O. and Jacob, D. J.: Ambiguity in the causes for decadal trends in atmospheric
960 methane and hydroxyl, *Proc Natl Acad Sci USA*, 114(21), 5367–5372, doi:10.1073/pnas.1616020114, 2017.
- 961 Turner, A. J., Frankenberg, C. and Kort, E. A.: Interpreting contemporary trends in atmospheric methane, *Proc Natl Acad Sci*
962 *USA*, 116(8), 2805–2813, doi:10.1073/pnas.1814297116, 2019.
- 963 Warwick, N. J., Cain, M. L., Fisher, R., France, J. L., Lowry, D., Michel, S. E., Nisbet, E. G., Vaughn, B. H., White, J. W. C.,
964 and Pyle, J. A.: Using $\delta^{13}\text{C}\text{-CH}_4$ and $\delta\text{D}\text{-CH}_4$ to constrain Arctic methane emissions, *Atmos. Chem. Phys.*, 16, 14891–14908,
965 <https://doi.org/10.5194/acp-16-14891-2016>, 2016.
- 966 Wecht, K. J., Jacob, D. J., Frankenberg, C., Jiang, Z. and Blake, D. R.: Mapping of North American methane emissions with
967 high spatial resolution by inversion of SCIAMACHY satellite data: NORTH AMERICA METHANE EMISSION
968 INVERSION, *J. Geophys. Res. Atmos.*, 119(12), 7741–7756, doi:10.1002/2014JD021551, 2014.



- 969 Worden, J. R., Bloom, A. A., Pandey, S., Jiang, Z., Worden, H. M., Walker, T. W., Houweling, S. and Röckmann, T.: Reduced
970 biomass burning emissions reconcile conflicting estimates of the post-2006 atmospheric methane budget, *Nat Commun*, 8(1),
971 2227, doi:10.1038/s41467-017-02246-0, 2017.
- 972 Zavala-Araiza, D., Herndon, S. C., Roscioli, J. R., Yacovitch, T. I., Johnson, M. R., Tyner, D. R., Omara, M. and Knighton,
973 B.: Methane emissions from oil and gas production sites in Alberta, Canada, *Elem Sci Anth*, 6(1), 27,
974 doi:10.1525/elementa.284, 2018.
- 975 Zona, D., Gioli, B., Commane, R., Lindaas, J., Wofsy, S. C., Miller, C. E., Dinardo, S. J., Dengel, S., Sweeney, C., Karion,
976 A., Chang, R. Y.-W., Henderson, J. M., Murphy, P. C., Goodrich, J. P., Moreaux, V., Liljedahl, A., Watts, J. D., Kimball, J.
977 S., Lipson, D. A. and Oechel, W. C.: Cold season emissions dominate the Arctic tundra methane budget, *Proc Natl Acad Sci*
978 USA, 113(1), 40–45, doi:10.1073/pnas.1516017113, 2016.